Genesis of the Goshen County, Wyoming, Tornado on 5 June 2009 during VORTEX2

KAREN KOSIBA AND JOSHUA WURMAN

Center for Severe Weather Research, Boulder, Colorado

YVETTE RICHARDSON AND PAUL MARKOWSKI

Department of Meteorology, The Pennsylvania State University, University Park, Pennsylvania

PAUL ROBINSON

Center for Severe Weather Research, Boulder, Colorado

JAMES MARQUIS

Department of Meteorology, The Pennsylvania State University, University Park, Pennsylvania

(Manuscript received 15 February 2012, in final form 29 August 2012)

ABSTRACT

The genesis of a strong and long-lived tornado observed during the second Verification of the Origins of Rotation in Tornadoes Experiment (VORTEX2) in Goshen County, Wyoming, on 5 June 2009 is studied. Mobile radar, mobile mesonet, rawinsonde, and photographic data are used to produce an integrated analysis of the evolution of the wind, precipitation, and thermodynamic fields in the parent supercell to deduce the processes that resulted in tornadogenesis. Several minutes prior to tornadogenesis, the rear-flank downdraft intensifies, and a secondary rear-flank downdraft forms and cyclonically wraps around the developing tornado. Kinematic and thermodynamic analyses suggest that horizontal vorticity created in the forward flank and hook echo is tilted and then stretched near the developing tornado. Tilting and stretching are enhanced in the developing low-level circulation as the secondary rear-flank downdraft develops, intensifies, and wraps around the circulation center. Shortly thereafter, the tornado forms. Tornadogenesis does not proceed steadily. Strengthening, weakening, and renewed intensification of the tornado are documented in photographic, reflectivity, Doppler velocity, and dual-Doppler fields and are associated with, and shortly follow, changes in the secondary rear-flank downdraft, convergence, location of the vortex relative to the updraft/downdraft couplet, tilting and stretching near and in the developing tornado, and the evolution of total circulation.

1. Introduction

Radar and in situ observations [e.g., Brandes 1978, 1984; Dowell and Bluestein 1997; Wakimoto et al. 1998; Trapp 1999; Wakimoto and Cai 2000; Dowell and Bluestein 2002a,b; Markowski et al. 2002 (MSR02); Beck et al. 2006; Wurman et al. 2007b (W07B), 2007c (W07C); Grzych et al. 2007 (G07); Marquis et al. 2008 (M08); Wurman et al. 2010 (W10); Marquis et al. 2012a (M12); Wurman et al. 2013], numerical simulations [e.g., Klemp and Rotunno 1983; Rotunno and Klemp 1985 (RK85); Wicker and Wilhelmson 1995 (WW95); Adlerman et al. 1999; Markowski et al. 2003], and theoretical studies (e.g., Davies-Jones and Brooks 1993; Davies-Jones et al. 2001) of tornadic and nontornadic supercells have advanced our knowledge of the processes necessary for tornadogenesis. But, the manner by which the finescale details of these processes and their interconnectivity *instigate* tornadogenesis is not well understood (see review papers by Davies-Jones et al. 2001; Markowski and Richardson 2009). In particular, the mechanism that ultimately triggers the rapid development and subsequent intensification of the near-surface rotation into a tornado is not known.

In an environment having only horizontal vorticity associated with the vertical wind shear, a downdraft is

Corresponding author address: Dr. Karen Ann Kosiba, Center for Severe Weather Research, 1945 Vassar Circle, Boulder, CO 80305. E-mail: kakosiba@cswr.org

DOI: 10.1175/MWR-D-12-00056.1

necessary, but not sufficient, for tornadogenesis. The vertical velocity gradients associated with an updraft alone could tilt rotation into the vertical, but would also carry it away from the surface. Vortex line configurations[1] observed near low-level (height $z <$ 1.0 km) mesocyclones suggest that downdrafts baroclinically generate and then, in conjunction with a proximal updraft, subsequently tilt horizontal vorticity $\boldsymbol{\omega}_h$ (the so-called *baroclinic* tornadogenesis mechanism; Davies-Jones et al. 2001) rather than simply rearranging and amplifying preexisting vertical vorticity (the so-called *barotropic* tornadogenesis mechanism; Davies-Jones et al. 2001; Markowski et al. 2003; Davies-Jones 2008; Parker 2012). Although the development of vertical vorticity at the surface is a prerequisite for tornadogenesis, many if not most nontornadic supercells also develop significant $\zeta[O(10^{-2})\ \mathrm{s}^{-1}]$ at the surface (Trapp 1999; Beck et al. 2006; Markowski et al. 2011), but fail to further amplify the ζ to tornado strength (typically 0.2–2 s^{-1}) (e.g., Wurman et al. 1996a; Wurman 2002; Alexander and Wurman 2005; Lee and Wurman 2005; W07B; W07C; M08; W10). A growing body of evidence suggests that the likelihood of tornadogenesis is significantly influenced by the thermodynamic characteristics of the rear-flank downdraft (RFD), with the likelihood of tornadogenesis decreasing as outflow becomes increasingly negatively buoyant (MSR02; G07; Hirth et al. 2008, hereafter H08), possibly because stretching of the ζ-bearing outflow air is inhibited (Markowski et al. 2003).

Numerical models (Adlerman 2003), finescale dual-Doppler (W07B; M08; W10) and mobile mesonet (G07; Finley et al. 2010, hereafter F10; Lee et al. 2011, hereafter L11) observations, and data assimilation experiments of tornado maintenance (M12) recently have revealed the presence of a secondary convergence line [secondary rear-flank gust front (SRFGF)] located behind the primary rear-flank gust front, which separates outflow air from inflow/environmental air (PRFGF). Others have noted multiple rear-flank gust fronts (F10; L11) and suggest that there may be differences in downdraft buoyancy during different stages in the evolution of a tornado. Vortex line analysis in the Crowell, Texas (2000), tornadic supercell suggested that a comparatively cold secondary rear-flank downdraft (SRFD)[2] might have assisted in maintaining an existing tornado by baroclinically generating and tilting $\boldsymbol{\omega}_h$ (M12). Data assimilation analyses for a different tornado (Argonia, Kansas; 2001) suggested that the SRFD surge might comprise relatively warm air, which was attributed to a heat burst–like mechanism. In situ observations by L11 during a weak tornado (Tipton, Kansas; 2008) indicated a relatively warm SRFD, which wrapped around the right flank of the tornado. A similar orientation was documented in the dual-Doppler analysis of other weakly tornadic storms (M12). In each of these storms, the SRFD may have contributed to convergence/divergence in, and hence the strengthening/weakening of, an already existing tornado. Although the kinematic and thermodynamic properties of several SRFDs (and their corresponding SRFGFs) have been documented, the relationship between the evolution of these properties, tornadogenesis, and subsequent intensification is unclear. Moreover, there are no microphysical and/or thermodynamic observations of SRFDs aloft, complicating the diagnosis of their origins.

The paucity of finescale, multiplatform integrated observations of both the kinematic and thermodynamic fields in supercells prior to and during tornadogenesis has hampered the unification of various findings. The second Verification of the Origins of Rotation in Tornadoes Experiment (VORTEX2) (Wurman et al. 2012, hereafter W12) provided an opportunity to collect such integrated data. This study focuses on the tornadogenesis period, 2148–2202 UTC (hereafter all times are UTC) 5 June 2009, of a long-lived (38 min) significant (EF2) tornado occurring in Goshen County, Wyoming, using data from two of the Doppler-on-Wheels mobile radars (DOW6, DOW7) (Wurman et al. 1997; Wurman 2001), a SMART radar (SR-2) (Biggerstaff et al. 2005), the Rapid-Scan DOW (Wurman and Randall 2001; Wurman et al. 2008), several mobile mesonets (MMs) (Straka et al. 1996; Waugh and Fredrickson 2010), rawinsondes, and photogrammetry teams (Wakimoto et al. 2011, 2012; Atkins et al. 2012). Through the integration of these data, the goal of this work is to document the kinematic, thermodynamic, and visual evolution of tornadogenesis and to examine the role

[1] The cyclonic low-level mesocyclone commonly is accompanied by an anticyclonic vortex that trails the hook echo (e.g., Brandes 1977, 1978, 1981, 1984; Fujita 1981; Fujita and Wakimoto 1982; Ray 1976; Ray et al. 1975, 1981; Heymsfield 1978; Klemp et al. 1981), with the two vorticity extrema being joined by vortex lines that arch upward and have a horizontal projection aligned with the buoyancy isopleths (Straka et al. 2007; Markowski et al. 2008, 2011; M12).

[2] In this work, the term SRFD is used to describe a downdraft region, behind the SRFGF. The semantic distinction of whether it is a distinct RFD or a pulse or intensification in an unsteady RFD phenomenon is not made. SRFD is used once the SRFGF is present. This region of downdraft/outflow behind the SRFGF has been referred to in other works using various terms, including "secondary surge" (W07B; M08; W10; M12).

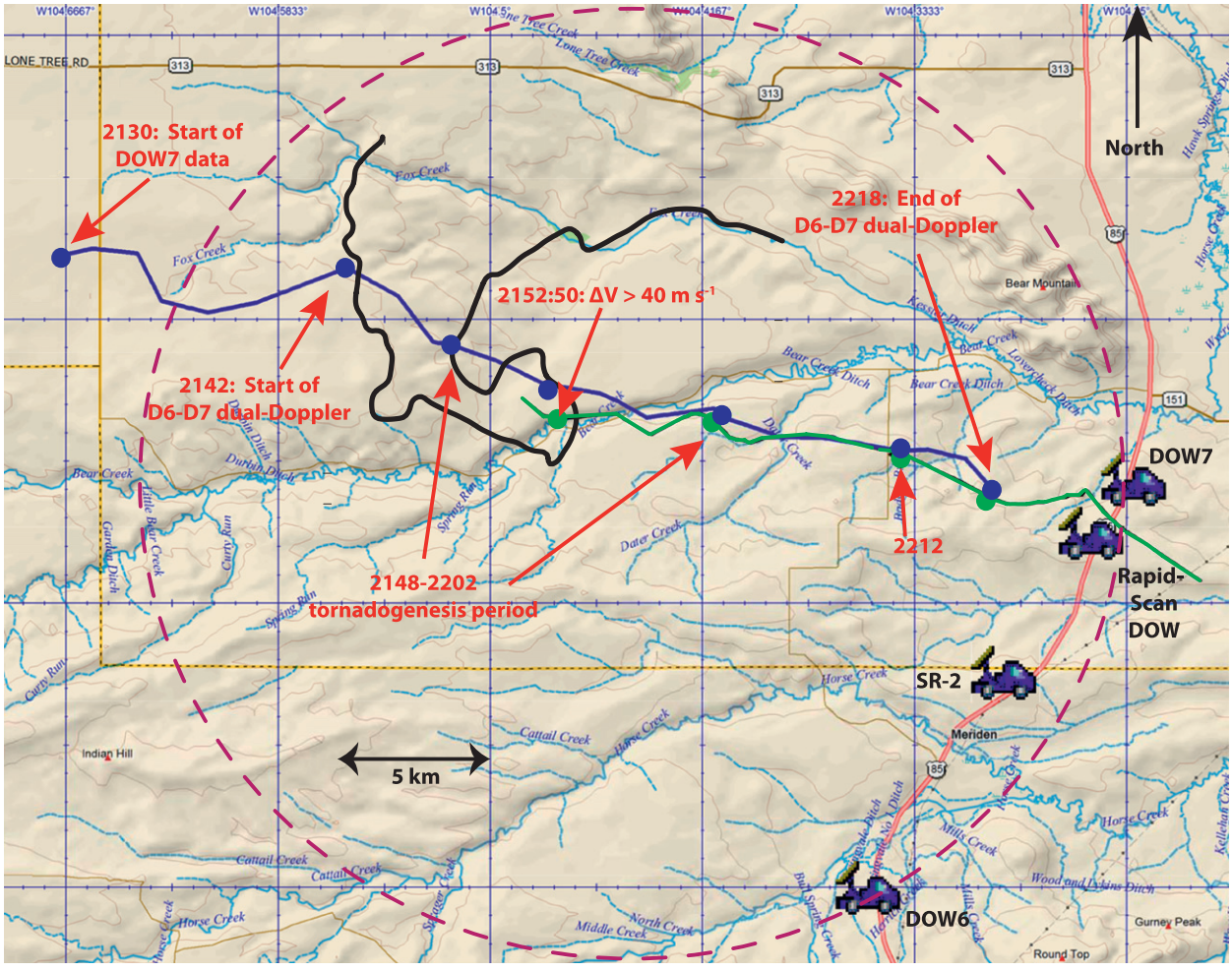

FIG. 1. Tracks of the mesocyclone at 1.5 km AGL (blue) and tornado locations (green) as measured by the DOW radars. The DOW6–DOW7 30° dual-Doppler lobe is indicated in purple and the 2152 DOW7 30-dBZ radar reflectivity isopleth in the hook-echo region is indicated in black. The location of the radars used in this study and selected reference times along the tornado/mesocyclone track are indicated.

of the RFD/SRFD in the tornadogenesis process. This is the third in a series of papers analyzing the life cycle of the Goshen County tornadic supercell, covering the pretornadic phase (2100–2148) (Markowski et al. 2012a,b), tornadogenesis (here), rapid intensification (2202–2212), and mature/dissipation phase (2212–2230) (Richardson et al. 2012). Analysis using data assimilation will be presented in Marquis et al. (2012b).

2. Overview of the DOW radar and mobile mesonet data collection

VORTEX2 deployed dozens of instruments before and during the time of tornadogenesis (W12). At 2129, DOW7 deployed along U.S. Highway 85 (41.61437°N, 104.25203°W), with the antenna center at 1488 m MSL, and began volumetric data collection at 2130. At this time, the tip of the hook echo of the supercell was 33.8 km distant at an azimuth of 286.0° from DOW7. At 2140, DOW6 also deployed along U.S. Highway 85 (41.495564°N, 104.347323°W), south and slightly west of DOW7, with the antenna center at 1568 m MSL, and began volumetric data collection at 2142 (Fig. 1). DOW6–DOW7 dual-Doppler data were available from 2142 to 2218. A detailed description of radar sampling and dual-Doppler techniques is provided in the appendix.

The MM carried roof-rack-mounted weather instruments, consisting of temperature sensors, an anemometer, a pressure sensor, a relative humidity sensor, and GPS, all sampling at 1-s intervals. They reached the forward-flank region by 2140 and the hook by 2155. Roads in this region were sparse and

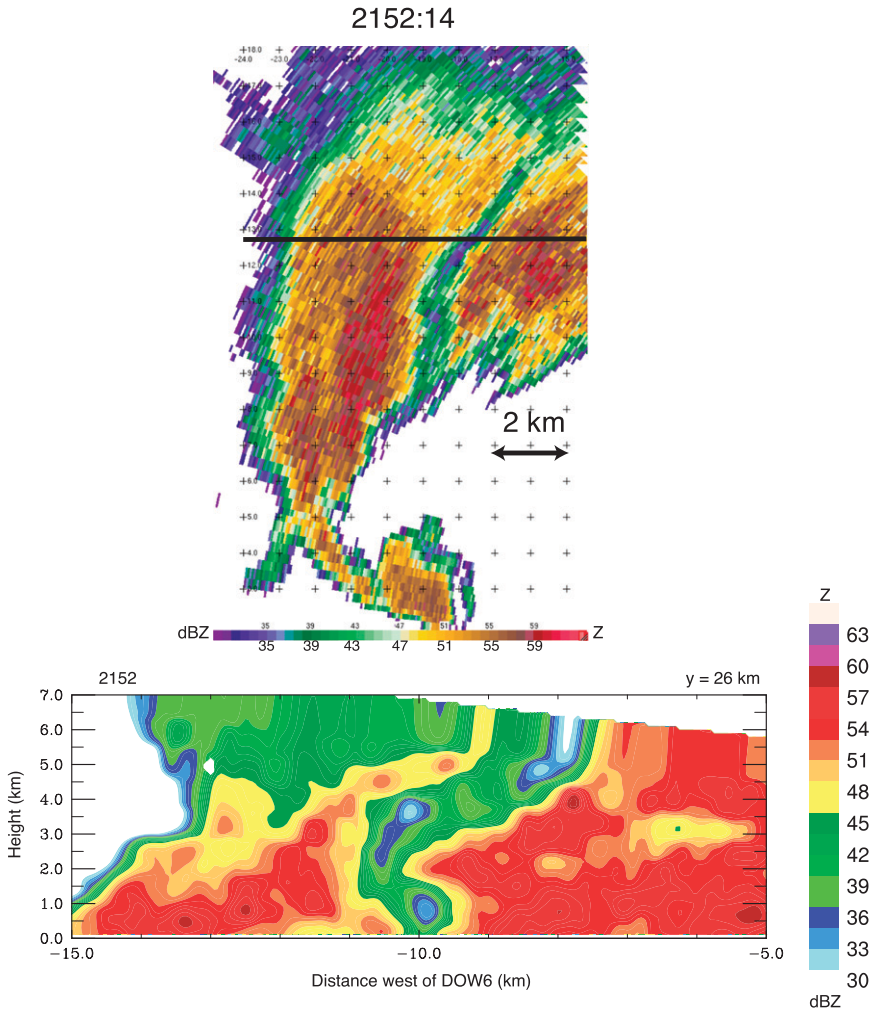

FIG. 2. (top) Expanded view of the LRR as viewed by DOW7 at 2152 and (bottom) a cross section through the LRR at the location of the black line. The LRR extended through the depth of the radar volume to at least 6 km.

predominantly unpaved. Initially, the MM could travel on unpaved roads, but after significant precipitation, they were limited to the paved Wyoming Highway 151 (WY151) and U.S. Highway 85 (US85). The MM targeted the gust fronts and outflow regions of the storm, given the potential importance of baroclinic vorticity generation and relative buoyancy in these regions.

3. Single-Doppler radar and photogrammetric observations

DOW observations starting at 2130 revealed a weak mesocyclone at $z \sim 1.2$ km (above radar level) coincident with a hook-shaped appendage (at this time, observations of the mesocyclone much below this level were precluded, owing to ground clutter). Attenuation of the radar reflectivity in the forward flank suggested the presence of hail, which was corroborated by MM observations at 2141. A low-reflectivity ribbon[3] (LRR) began to form between the forward and rear flanks of the storm and persisted through the genesis period (Figs. 2, 3). Between 2142 and 2148, simultaneous with the

[3] The LRR was a phenomenon first noticed in this storm, and subsequently in others (W12). LRRs were characterized by a narrow strip (~600 m in width) of reduced reflectivity (up to 25-dB deficit) and low differential reflectivity values separating the forward and rear flanks of the storm and extending upward to at least 6 km. In this storm, the LRR was not associated with any prominent wind field variations, and it did not appear to play a major role in the genesis of the Goshen County tornado. As will be discussed in the next section, parcels entering the tornado passed near but not through the LRR.

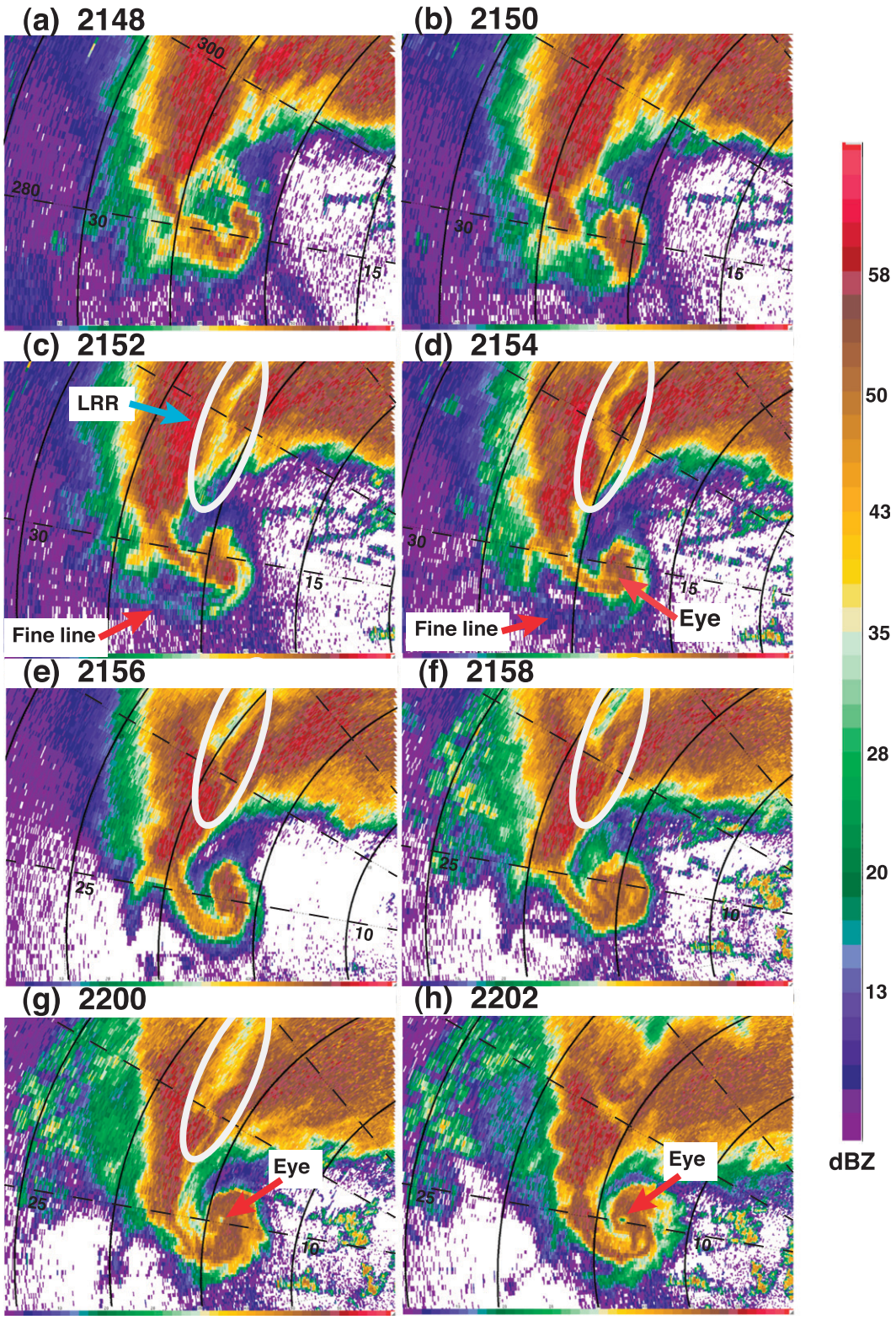

FIG. 3. (a)–(h) Evolution of the 1° elevation reflectivity field (shown every other sweep, every 2 min), as measured by DOW7, from 2148 to 2202. An LRR (white ellipse) reappeared near the time of tornadogenesis. A low-reflectivity eye was barely discernible at 2154, but became prominent at 2200 onward. Reflectivity in the knob of the hook increased, and the tip of the hook coiled into a classically tornadic appearance.

intensification of the developing low-level circulation, reflectivity increased west of the updraft and a descending reflectivity core (DRC) (e.g., Rasmussen et al. 2006; Byko et al. 2009) reached the surface (Markowski et al. 2012a). The reader is referred to Markowski et al. (2012a,b) for a detailed analysis of supercell evolution prior to 2148.

The reflectivity presentation of the knob of the hook echo dramatically evolved between 2148 and 2202, with reflectivity increasing both in magnitude and in coverage between 2148 and 2150 (Fig. 3). The development of a low-reflectivity eye occurred over several minutes, with an eye only barely visible before 2155, filled in from 2157 to 2159, and then becoming well defined and persistent by 2200 and thereafter. This formation, filling, and reformation of the eye were linked to measured changes in tornado intensity, discussed below.

Similar to earlier times (Markowski et al. 2012a), photographic observations indicated little to no visible precipitation below the (hook) cloud base or near the DRC during this time (Fig. 4). A funnel first became visible aloft at 2156:30 (Fig. 4d), but quickly dissipated and was no longer present by 2156:59 (see also Wakimoto et al. 2011). After this time, a broad lowering was visible, morphing into two broad lowerings between 2158 and 2159. After 2200, the funnel redevelops, lowering to near the ground by 2202:33. The formation, dissipation, and redevelopment of the funnel were linked to changes in tornado intensity, discussed below.

The Doppler velocity field underwent significant evolution between 2148 and 2202 (Fig. 5). Between 2148 and 2154, strong west–east (toward DOW7) flow developed to the south of the nascent tornado. This strong flow then wrapped cyclonically to the east and then north of the circulation (not visible in the single-Doppler fields, but confirmed in the dual-Doppler analyses). Further, at 2152, a weak, east–west-oriented wind shear/convergence line associated with the SRFGF (as additionally documented in the dual-Doppler analysis, discussed below) was discernible south and west of the developing tornado. This was evident as a fine line of enhanced reflectivity at 2154 (Figs. 3c,d). From 2152 to 2156, regions of implied anticyclonic ζ were evident to the south and southwest of the tornado (Figs. 5c–e). The region of anticyclonic ζ also was visible as a cloud lowering south of the developing tornado from 2152 to 2159 (Figs. 4b–e). These anticyclonic Doppler velocity features became difficult to discern from 2157 to 2159, then again were evident from 2200 to 2202, but not visually (Fig. 4f). The location of the anticyclonic vortices suggested they were positioned along/near the east–west-oriented convergence line, which will be discussed in more detail in the context of the dual-Doppler analysis. Apparent divergence, inferred from the change in Doppler velocity with range

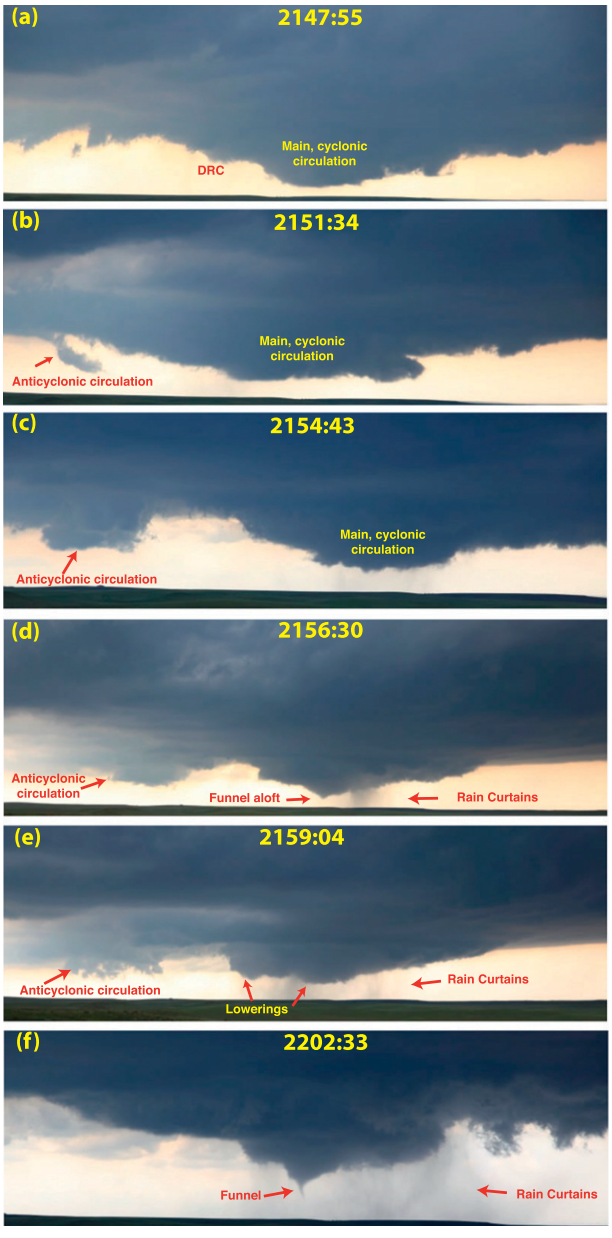

FIG. 4. (a)–(f) Visual evolution of the storm structure during the tornadogenesis period. Cloud-base lowerings associated with cyclonic and anticyclonic circulations that were evident in the radar wind fields are annotated. Photographs were taken from the DOW7 location looking east-southeast [courtesy of N. Atkins and R. Wakimoto (Lyndon State University/National Center for Atmospheric Research photogrammetry team)].

(and confirmed by dual-Doppler analysis), associated with the RFD became increasingly prominent from 2158 to 2202, suggesting an increase in downdraft strength (Figs. 5f–h).

As a measure of tornado strength, the Doppler velocity difference across the low-level circulation/tornado (ΔV) from the 1.0° tilts was analyzed as a function of time for

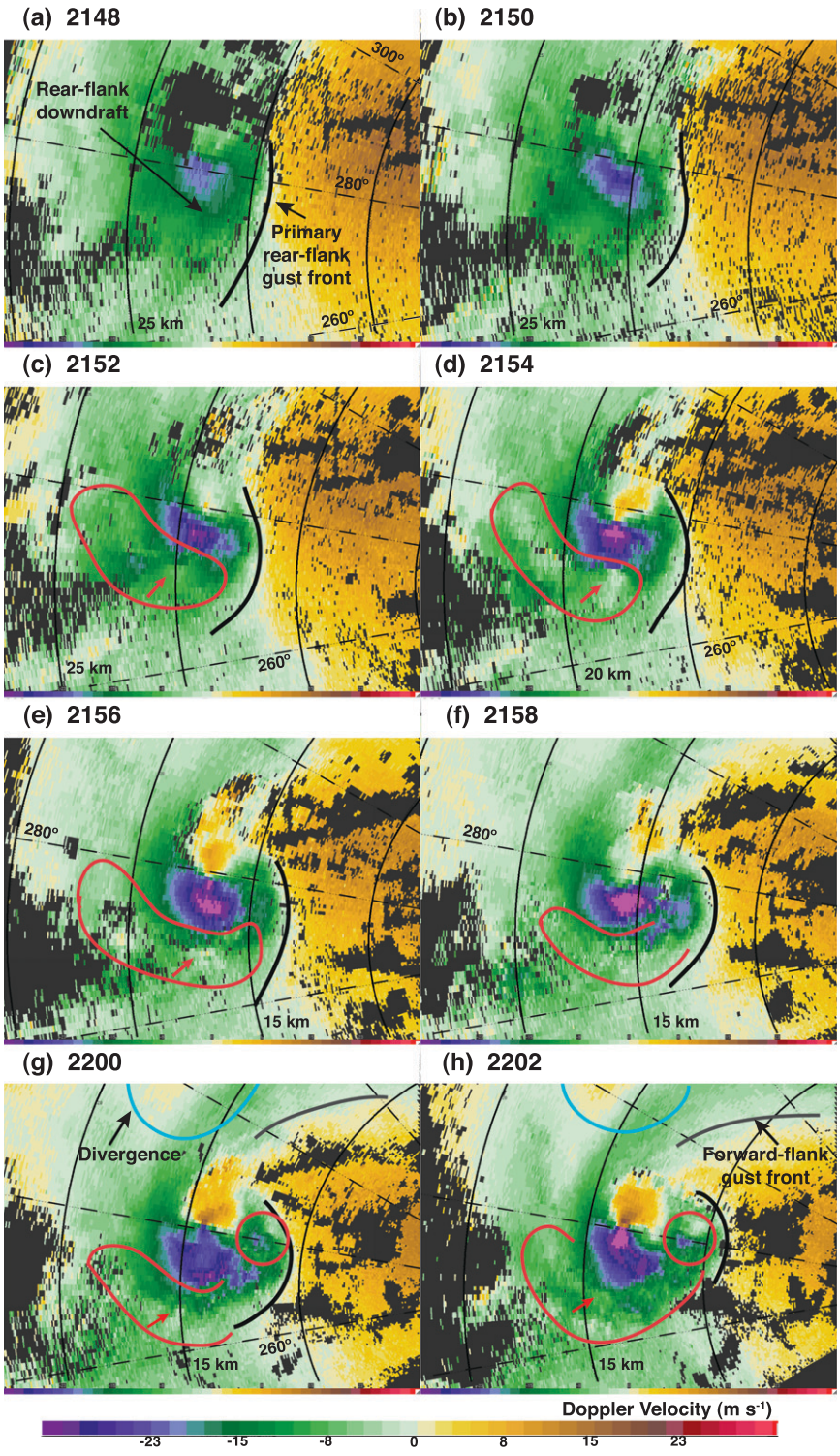

FIG. 5. (a)–(h) Evolution of the Doppler velocity field at 1° elevation as measured by DOW7 (shown every 2 min). By 2152:50 (not shown), the velocity difference across the couplet exceeds 40 m s^{-1}, the tornadic threshold established by Alexander and Wurman (2008). Between 2152 and 2202, the RFD wraps east of the tornadic circulation. Red arrows indicate anticyclonic regions, red curves delineate the SRFD and SRFGF region, red circles indicate a secondary cyclonic region, and blue curves denote a region of increasing divergence extending north of the displayed panels.

DOW6, DOW7, Rapid-Scan DOW, and SR-2 (Fig. 6).[4] Winds first exceeded the $\Delta V = 40$ m s^{-1} tornadic threshold (as defined by Alexander and Wurman 2008) just after 2152 and remained above this threshold until 2158. The winds became briefly and marginally subtornadic at 2159, but by the next low-level scan at 2200, ΔV exceeded 40 m s^{-1}. DOW measurements indicated that the tornado began well before a condensation funnel reached the ground after 2202 (Fig. 4), consistent with observations in weak tornadoes (e.g., Wurman et al. 2007c).

The DOW7 ΔV increased to 60 m s^{-1} by 2203, weakened to 53 m s^{-1} by 2207, then increased to 93 m s^{-1} at 2212, after which time there was only a modest increase in ΔV, peaking at 104 m s^{-1} near 2217 (108 m s^{-1} in the 0.5° scans).[5] The Rapid-Scan DOW measured Doppler velocities of up to 72 m s^{-1} and a ΔV of 121 m s^{-1} at 15–20 m AGL just after 2220. At 2211:13, the Tornado Intercept Vehicle (Wurman et al. 2007a) measured winds of 58 m s^{-1} at 3 m AGL as the tornado crossed 4 Corners Road, with winds on the south-southwestern side of the tornado breaking several telephone poles before the poles experienced the peak observed winds in the southwestern sector (Wurman et al. 2013). The National Weather Service, which had issued a tornado warning at 2127, 25 min ahead of the genesis time determined by ΔV, rated this tornado an EF2, based partially on these DOW and in situ observations.[6]

Since the low-level structure of the tornado was observed every minute of its life, and every 7 s by the Rapid-Scan DOW after 2202, it was possible to provide a precise track of the tornado (Fig. 1). Just after 2152, when the developing tornado first surpassed $\Delta V = 40$ m s^{-1}, the circulation center was located over Bear Creek and just north of Bear Creek Road (41.638°N, 104.473°W). The center of circulation crossed Bear Creek Road at 2157, at which time peak low-level (inbound) Doppler velocities were 43 m s^{-1}. The tornado moved generally southeastward until 2219. After 2219, the tornado narrowed considerably, while maintaining ΔV near 100 m s^{-1}. It crossed US85 (41.6080°N, 104.2563°W) at 2225:42, only 400 m north of the Rapid-Scan DOW, while weakening rapidly, and then dissipated at 2230 near 41.590°N, 104.221°W. [Details concerning the evolution of the tornado after genesis are provided in Richardson et al. (2012).] There was a suggestion of a cycloidal nature to the path of the tornado, with maximum departure of the vortex center from the mean mesocyclone path occurring at 2154 and 2202.

4. Dual-Doppler and thermodynamic analysis

The evolution of the low-level (0.3-km grid level)[7] winds and ζ derived from the DOW6–DOW7 dual-Doppler synthesis between 2148 and 2202 is shown in Fig. 7 (see appendix for the dual-Doppler methodology). At 2148, an RFD, with an associated PRFGF oriented in a northeast–southwest line, was west and southwest of the low-level circulation center. To quantify downdraft strength, average w values were calculated over 0.25-km^2 regions west and east of the developing tornado enclosing the strongest portions of the downdrafts, as shown in Fig. 7. Necessarily, the exact location of the averaging boxes changed for each analysis time because of the evolution of these features. From 2148 to 2150, the magnitude of the peak downward vertical velocities, w, associated with the RFD had increased (Fig. 8) and an SRFGF, as evidenced by an increase in low-level convergence/upward motion, developed south and west of the low-level circulation center [SRFGF from (−13.5, 15) to (−20, 16.2) at 2150 in Fig. 7b]. Through 2154, the SRFD expanded horizontally eastward and became stronger east of the developing tornado. East of the tornado, peak SRFD velocities increased between 2152 and 2154, decreased to a relative minimum at 2156, and increased again through 2158–2200. Peak resolved convergence and stretching (calculated over 0.25-km^2 regions enclosing the strongest values of convergence and stretching) proximate to the center of the developing tornado tracked with and slightly lagged changes in SRFD intensity, increasing from 2148 to 2154, decreasing until 2158, and then increasing again through 2202. Changes in developing tornado intensity tracked (with a slight lag) these metrics, increasing from 2148 to 2156, decreasing until 2159, and then increasing through 2202.[8] It should be noted that these metrics are calculated

[4] Often two spatial scales of circulation were present, with an inner subkilometer scale embedded inside a 1–2-km-scale circulation (e.g., Wurman et al. 1996a,b; Wurman and Gill 2000; Wurman 2002; Kosiba and Wurman 2008). For calculations of ΔV, the inner persistent circulation was selected.

[5] The ΔV calculations were affected strongly by the various radars' abilities to resolve the core flow region of the evolving tornado, which shrank from ~1000 to 300 m during genesis.

[6] The 72 m s^{-1} measured by the Rapid-Scan DOW was very near the EF3/EF4 threshold, but the tornado passed through an area devoid of damage indicators at the time of the measurement. This observation was not available to the National Weather Service at the time they made the EF-scale rating. DOW7 measured winds of 62 m s^{-1} at heights as low as 31 m AGL at an earlier time.

[7] See appendix for definition of height coordinate over the variable height terrain; hereafter all heights refer to grid levels unless AGL is indicated.

[8] While metrics associated with increases in tornado intensity decreased from 2156 to 2158, they did not become negative prior to the tornado weakening. While not diagnosed, dissipative effects likely are always present. It is surmised that during 2156–2158, dissipative effects dominated processes causing tornado intensification, therefore the tornado weakened.

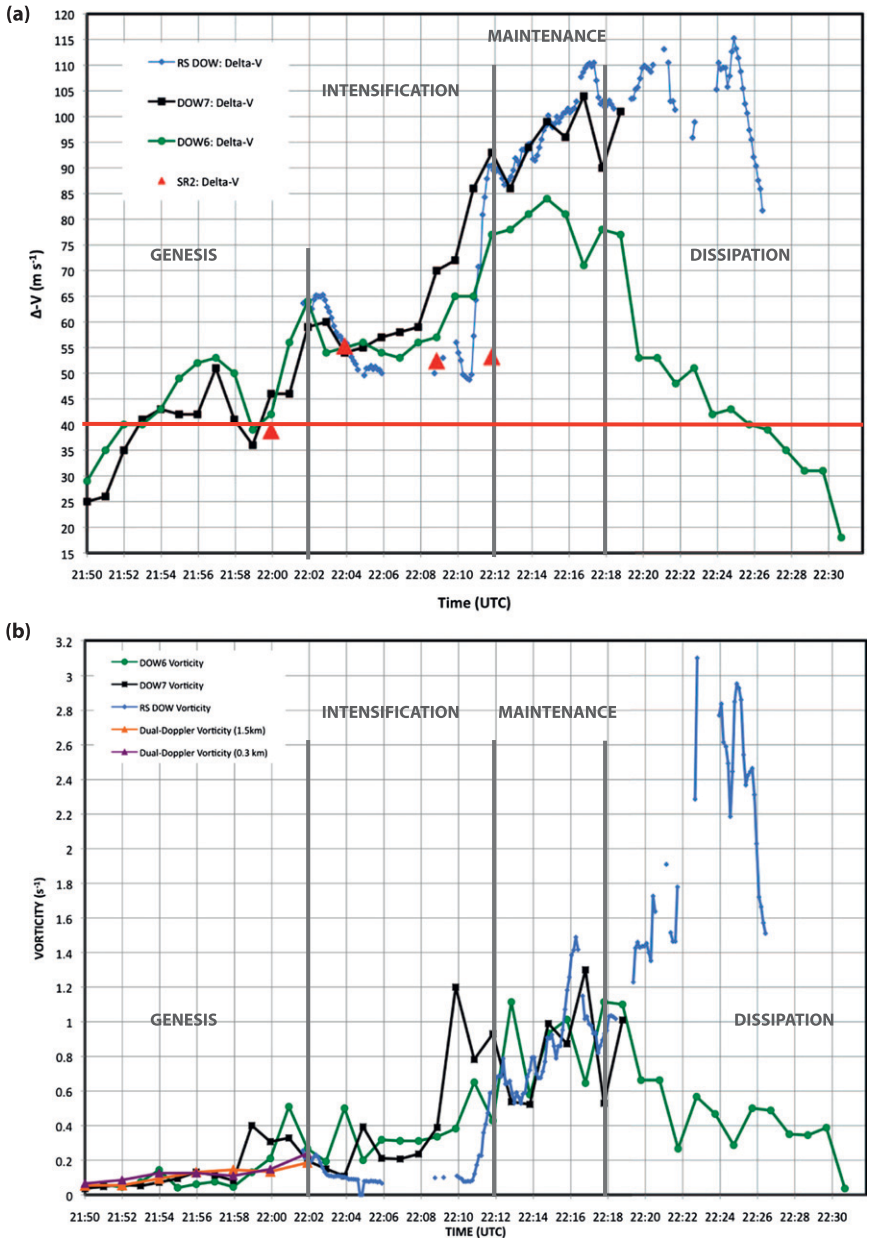

FIG. 6. (a) Evolution of the low-level ΔV (solid lines) as measured by DOW7 (black line), DOW6 (green line), Rapid-Scan DOW (blue line), and SR-2 (red triangles). The ΔV from the DOW6 and DOW7 radars exceeded the 40 m s^{-1} tornado threshold after 2152 and approached 50 m s^{-1} by 2157. At 2159, ΔV briefly dropped several m s^{-1}, to below 40 m s^{-1} before a rapid increase until 2212, then remained relatively constant until 2217, and then decreased. (b) Evolution of ζ as deduced from DOW7 (black line), DOW6 (green line), and Rapid-Scan DOW (blue line) measurements and from the dual-Doppler synthesis in this study at heights of 0.3 km (purple line) and 1.5 km (orange line). A 5-point smoother was applied to the Rapid-Scan DOW observations.

from data collected nearly contemporaneously at synthesis altitudes primarily from the lowest radar tilts, obtained during the initial 30 s of each radar volume, so they represent short-duration snapshots at intervals of 2 min. The relationships among these metrics and others, including the evolution of circulation, will be discussed below.

The RFD and PRFGF were coherent through at least $z = 3.0$ km, above which height the retrieved vertical velocities were noisy (not shown). The SRFGF was

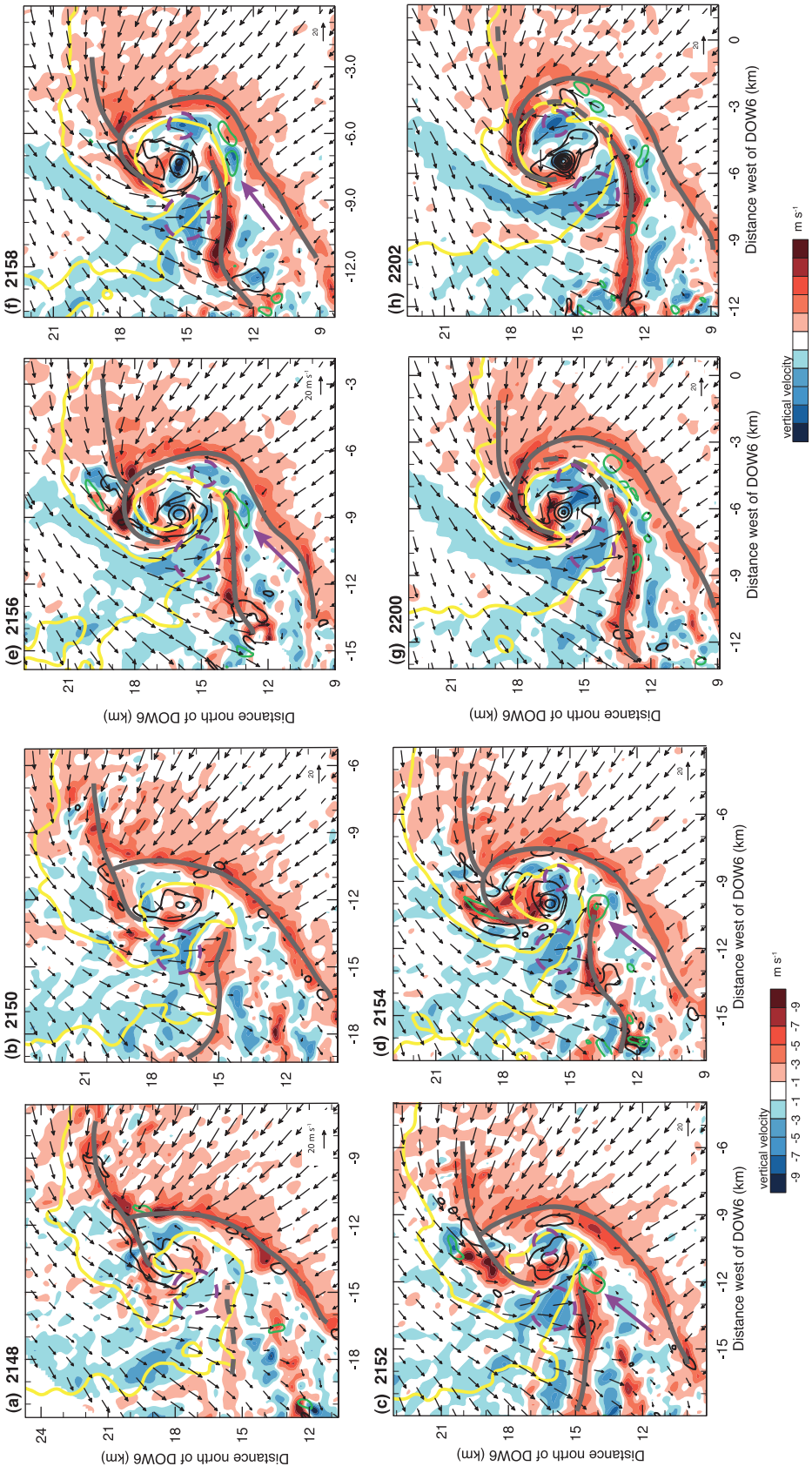

FIG. 7. (a)–(h) Dual-Doppler winds at 0.3 km AGL from 2148 to 2202. Yellow contours depict the 30-dBZ DOW7 reflectivity isopleth, vectors represent the horizontal winds, shading depicts w, black contours depict $\zeta > 0.02\ s^{-1}$, and green contours depict $\zeta < -0.02\ s^{-1}$ contoured every $0.04\ s^{-1}$. The PRFGF, FFGF, and SRFGF are delineated by solid gray lines. Dashed gray lines indicate uncertainty in position. The dashed circles outline the approximate locations of where the RFD/SRFD downdraft metrics were calculated. Purple arrows indicate the region of prominent anticyclonic ζ, south of the hook.

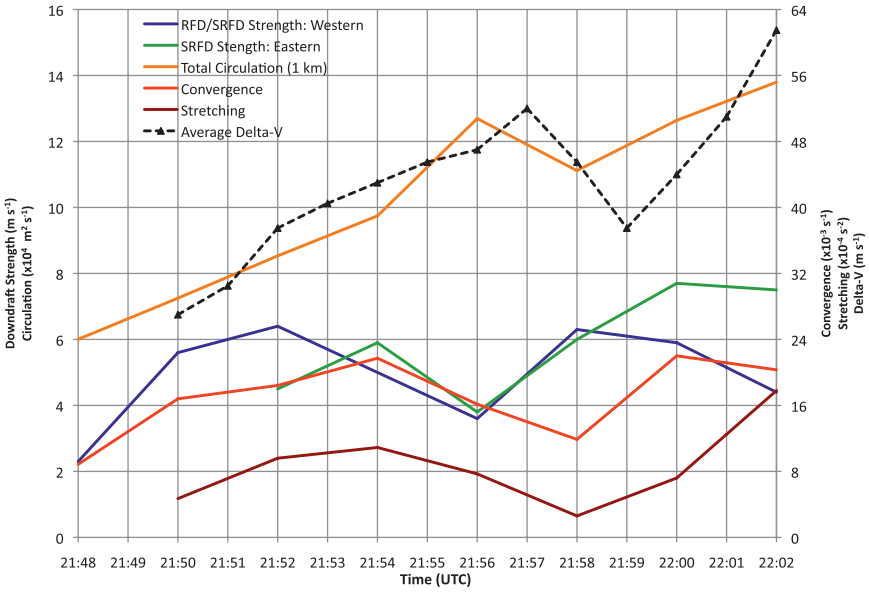

FIG. 8. Magnitude of the RFD/SRFD, the cyclonically eastward-northeastward wrapping SRFD, convergence, stretching, and circulation at 1-km radius from the developing tornado as a function of time. Also shown is average ΔV from the DOW6 and DOW7 radars, a measure of tornado intensity. Changes in tornado intensity closely track, with a lag, changes in the other metrics.

coherent through $Z = 1.5$ km, but was difficult to discern at higher altitudes, as the magnitude of the SRFGF relative to the PRFGF diminished with height (Fig. 9). From $Z = 0.3$ to 1.5 km, the PRFGF sloped backward (to the west-northwest) with height, suggesting that the RFD air was less buoyant than the surface air it was replacing, whereas the SRFGF did not appear to slope much with height, perhaps indicating that SRFD buoyancy was comparable to that of the original RFD during the genesis time period (Fig. 10).[9] As discussed below, there were no MM observations across the PRFGF or SRFGF during tornadogenesis, thus these hypotheses could not be evaluated.

From 2150 to 2154, low-level (Z = 0.3 km) peak cyclonic ζ associated with the developing tornado increased to over 0.1 s^{-1}, remained constant from 2154 to 2156, decreased slightly at 2158, and then increased to over 0.15 s^{-1} from 2200 onward, remaining near 0.2–0.3 s^{-1} through 2212 (Fig. 6b). This was similar to the values calculated from dual-Doppler analyses in a variety of weak and strong tornadoes (0.1–0.4 s^{-1}) (W07B; W07C; M08; W10), and to the single-Doppler ζ values for this case. While observational geometries, radar resolutions, scanning strategies, and smoothing parameters were somewhat different among all these studies, the qualitative agreement among these calculated quantities enhanced confidence that similar scales/phenomena had been resolved and that the results from these various studies could be compared meaningfully. From 2150 to 2154, secondary regions of cyclonic ζ, with typical values of 0.02 s^{-1}, were evident to the north of the tornadic circulation and triple point of the RFGF and the forward-flank gust front (FFGF), but became less evident after 2156 (Fig. 7). Such enhancements in ζ had been associated with cyclic tornadogenesis (Adlerman et al. 1999), but also with cases (W07B; W07C)—including this one—where cyclic tornadogenesis was not observed.

Aloft (z = 1.5 km), at 2148, a prominent region of anticyclonic ζ (−0.04 s^{-1}) was present just south of the rear–forward flow associated with the strengthening RFD [located at (−15, 16.5) in Fig. 9a]. This region of anticyclonic ζ was coincident with a commonly observed reflectivity flare on the southern portion of the hook (e.g., Markowski 2002; Kosiba and Wurman 2008). By 2152, anticyclonic ζ was evident in the wind fields near the surface (0.3 km) [located at (−12, 14.5) in Fig. 7c], concentrated initially just south of, then on, the SRFGF and adjacent to the strong rear–front flow. Vortex lines (discussed in more detail below) formed arches between these regions of anticyclonic ζ and the cyclonic ζ maximum located near the developing tornado.

[9] The slopes of gust front updrafts are also influenced by vertical wind shear, and the slope represents an imbalance between shear and relative buoyancy, but in general, relatively less-buoyant outflows would tend to undercut more-buoyant air masses.

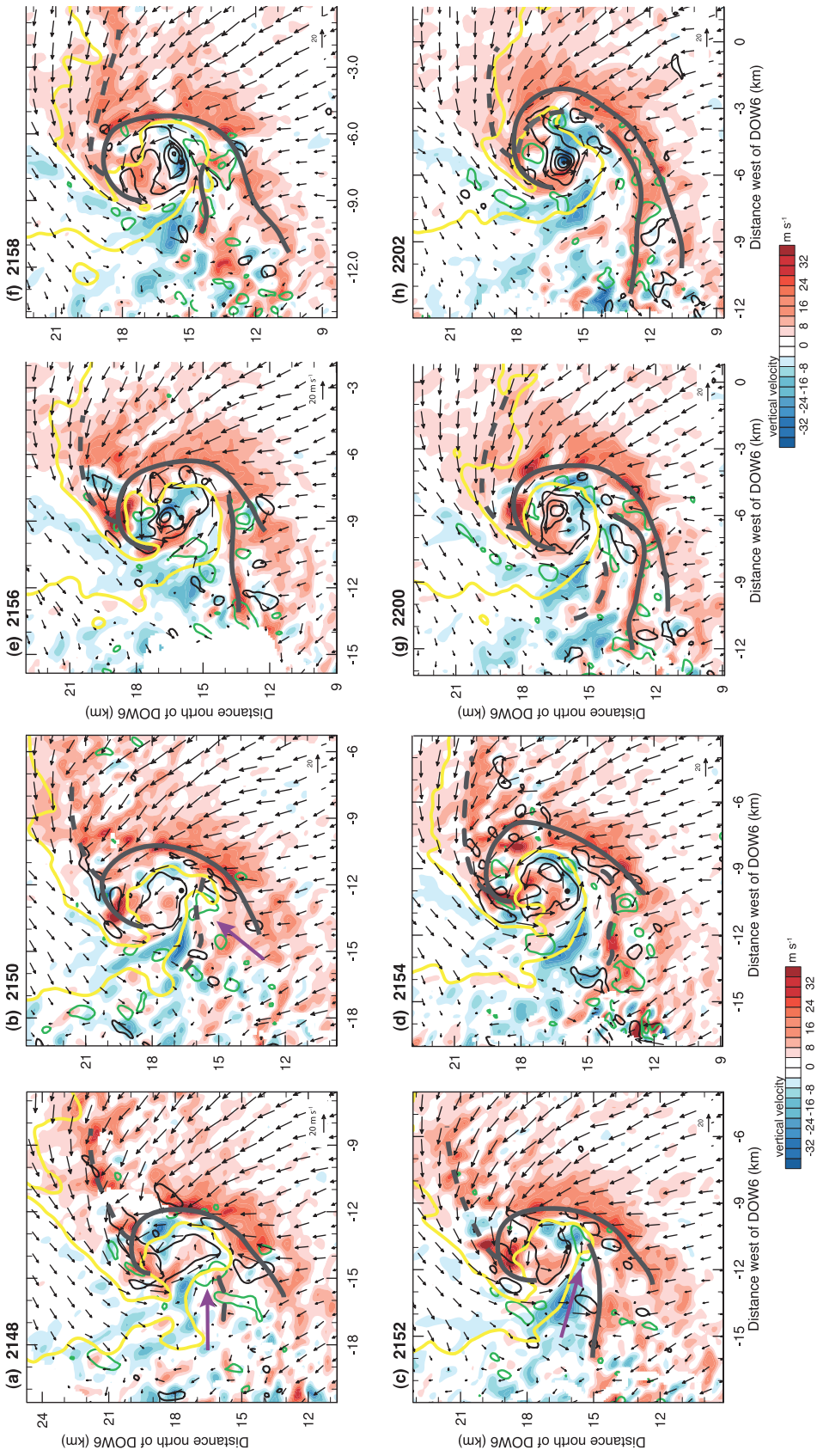

FIG. 9. As in Fig. 7, but at a height of 1.5 km.

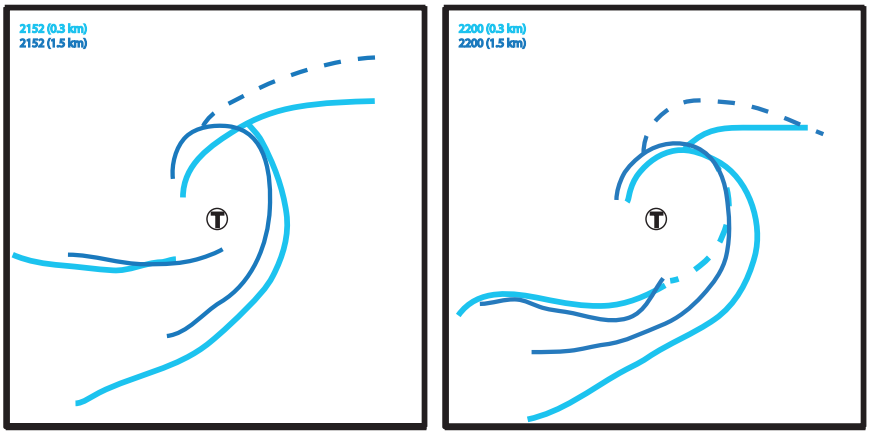

FIG. 10. Locations of the gust fronts at the surface (0.3 km; light blue) and aloft (1.5 km; dark blue) for (left) 2152 and (right) 2200 relative to the tornado (T). The FFGF and PRFGF slope backward with height, whereas the SRFGF does not exhibit much slant with height, possibly indicating differences in relative buoyancies across the different boundaries.

During genesis, the mesocyclone exhibited a divided vertical velocity structure (Lemon and Doswell 1979) as the downdraft reached the surface and wrapped cyclonically around the low-level updraft. The low- and midlevel ζ maximum, originally centrally located in the updraft (at $z = 0.3$ and 1.5 km), was located in the updraft but closer to the updraft/downdraft interface at all times except 2158 (Figs. 7, 9). At 2158, the ζ maximum was located well within the downdraft region (at both $z = 0.3$ and 1.5 km), where vorticity compression is present; during this time tornado intensity decreased (Fig. 8). By 2200, the ζ maximum returned to the updraft near the updraft/downdraft interface, and tornado intensification resumed. While the exact location of the vertical vorticity maximum relative to the downdraft interface is sensitive to the wind synthesis parameters, peak resolved convergence decreased from 2156 to 2158 and then again increased from 2158 to 2200, suggesting that trends in resolved convergence are associated with trends in subgrid-scale convergence and hence tornado intensity.

From 2148 to 2156, the magnitude of horizontal vorticity was enhanced along the PRFGF [located from (−12.0, 12.0) to (−12.0, 20.0) in Fig. 11a] and near the developing SRFGF [located from approximately (−12.5, 15) to (−18.0, 15.0) in Fig. 11a]. Regions of weaker horizontal vorticity were concentrated near the FFGF to the immediate west and north of the developing tornado. MM observations of virtual potential temperature θ_v revealed baroclinic zones within the rear- and forward-flank downdrafts consistent with the dual-Doppler analysis of enhanced $\boldsymbol{\omega}_h$ in these regions (that could then be converted to ζ by later tilting and stretching). The θ_v deficit (relative to storm inflow) was small near the forward-flank downdraft (FFD) and RFD regions (θ_v decreases from 309 K east of the hook to 306–307 K in the knob of the hook and in the forward flank). This finding was consistent with the observations of MSR02 and G07, who noted that the outflow within 4 km of the circulation center of significantly tornadic supercells had smaller θ_v deficits (≥ -3.0 K) than nontornadic or weakly tornadic supercells. However, the coarseness of the MM observations precluded evaluation of temporal and finescale spatial changes in baroclinicity and no observations existed across the SRFGF during tornadogenesis.

To examine further the origins of the observed vorticity, vortex lines were constructed near the surging downdraft, starting at $z = 0.3$ km at the location of the anticyclonic ζ maximum that was adjacent to the SRFGF.[10] From 2152 to 2156 (Figs. 11a, 12a), the vortex lines arched upward, connecting to regions of cyclonic ζ along the PRFGF and near the southern portion of the developing tornado. This morphology was suggestive of the generation of baroclinic $\boldsymbol{\omega}_h$, as proposed by Straka et al. (2007), in which a negatively buoyant downdraft baroclinically generates vortex rings that subsequently are tilted by the horizontal gradient of vertical velocity encountered as they are advected forward during their descent by the rear–front flow through the region of negative buoyancy. Vortex lines at 2158,

[10] Vortex lines passing through the center of cyclonic ζ did not arch, but instead extended vertically through the depth of the dual-Doppler analysis domain. This lack of arching may be due in part to the inability to capture the apex of the arches, as they extend to such high altitudes, or baroclinic and/or turbulent processes that have modified their structure (Markowski et al. 2008). It also is possible that the processes that contributed to producing the main cyclonic circulation occurred prior to this time period and thus were not represented in the current analysis.

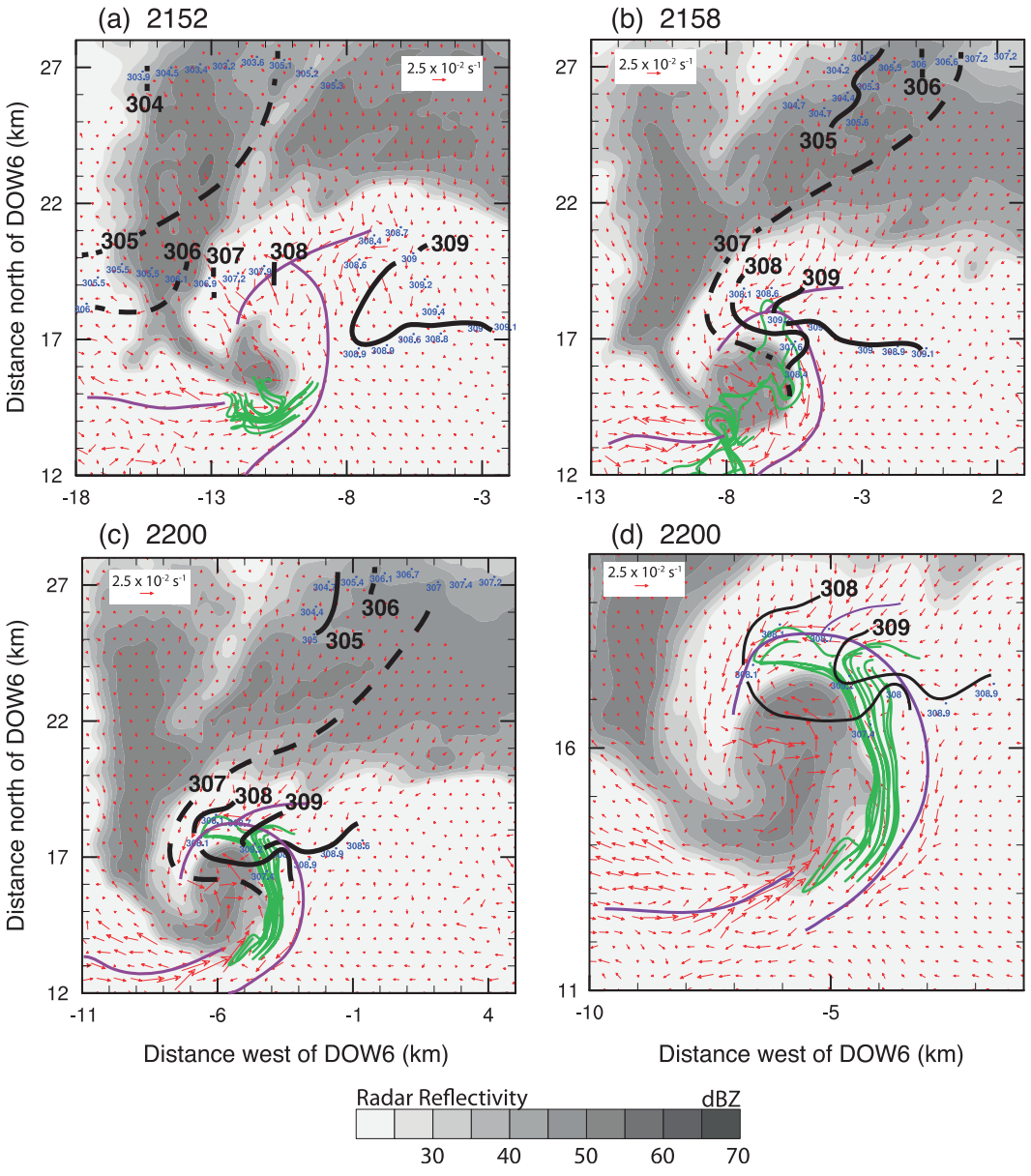

FIG. 11. Virtual potential temperature (black subjectively drawn contours) calculated from MM observations (blue numbers) relative to the 0.3-km DOW7 reflectivity (grayscale) and 0.3-km dual-Doppler derived $\boldsymbol{\omega}_h$ (red vectors) for (a) 2152, (b) 2158, and (c) 2200, and (d) a close-in view of the hook at 2200. MM observations are presented for a 5-min time period, centered on the nominal time. The green lines are horizontal projections for the vortex lines constructed near the secondary downdraft surge. Purple lines denote the locations of the PRFGF and SRFGF. The θ_v contours indicate regions of baroclinicity near the FFGF and the RFGF. Horizontal vorticity at a height of 0.3 km also is appreciable in these regions. Vortex lines at 2152 and 2200 connect regions of anticyclonic and cyclonic vorticity located near the PRFGF and SRFGF, respectively, whereas at 2158, vortex lines are not observed between these regions.

while the tornado was weakening, were unlike earlier and later arch structures (Figs. 11b, 12b). They were not well connected between regions of cyclonic and anticyclonic low-level ζ, and do not have an arch-shaped appearance. Possible explanations for this pattern include transient changes in downdraft buoyancy gradients and/or convergence, which potentially would alter vorticity production and orientation. By 2200, as the tornado resumed intensifying, the arch pattern was reestablished (Figs. 11c, 12c).

To convert this horizontal vorticity into vertical vorticity, the tilting of horizontal vorticity into the vertical

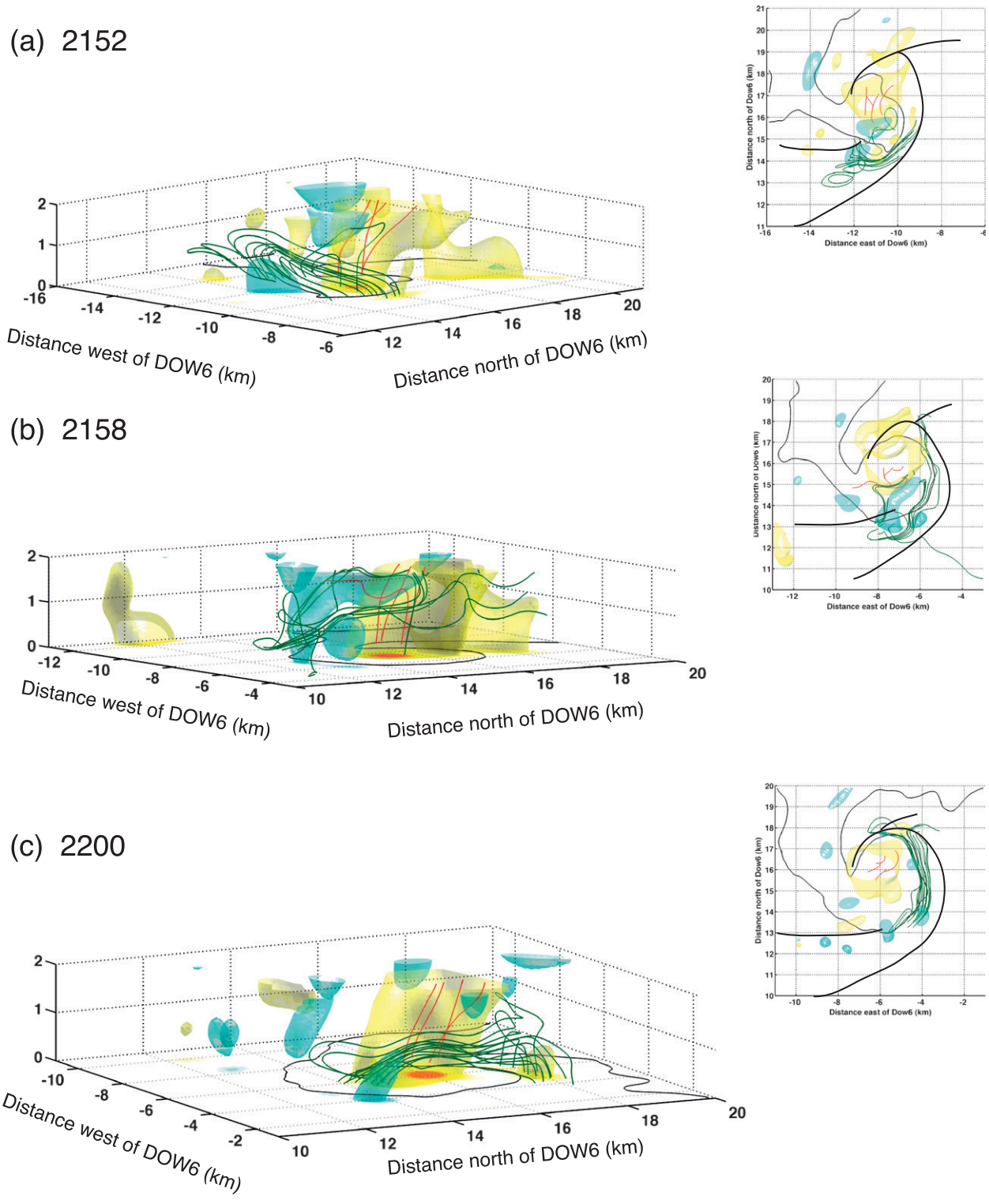

FIG. 12. Vortex lines at (a) 2152, (b) 2158, and (c) 2200, illustrating an arched pattern from near the PRFGF and the SRFGF at 2152 and 2200 and no arching at 2158 (green). Vortex lines originating in the center of the developing tornado (red) rise to high altitudes. Cyclonic (yellow) and anticyclonic (blue) ζ isosurfaces (0.02 s^{-1}) are contoured.

(tilting hereafter) likely occurred as air approached the ζ center. Tilting experienced by parcels moving toward the tornado was difficult to correlate with observed changes in ζ experienced by these same parcels, even with these, and other, finescale dual-Doppler data (W07B; W07C; M08; W10).[11] However, the evolution of prominent features in the instantaneous tilting fields was well correlated with changes in storm structure (e.g., visually observed funnels, development of a low-reflectivity eye) and tornado intensity (Figs. 8, 13). Strong tilting was present in the immediate vicinity of the developing/intensifying tornado (2150–2154, 2200) and was weaker in the same region as tornado intensity decreased (2156–2158). A broad region of weaker tilting, concentrated along the PRFGF and FFGF, was present prior to and during the tornadogenesis period.[12] The stretching of ζ associated with the developing tornado increased from 2148 to 2154, decreased through 2158, and again increased through 2202, correlated with changes in tornado intensity (Fig. 8).

Changes in the intensity of the developing tornado shortly followed changes in downdraft intensity associated with the secondary surge and related changes in convergence, tilting, and stretching. In the absence of evidence of changes in the production of $\boldsymbol{\omega}_h$ during tornadogenesis, this correlation suggested that the eastward surging SRFD enhanced ζ through increased tilting and stretching at the surge/updraft boundary proximate to the tornado.

Circulation and trajectory analysis

Changes in the low-level circulation were evaluated further through circulation and trajectory analysis. The total low-level circulation ($C_{z=0.3\text{km}} = \oint \mathbf{v} \cdot \mathbf{dl}$, where $\mathbf{v}$ is dual-Doppler-determined velocity and $\mathbf{l}$ is distance along the boundary of the region over which C is being calculated) was calculated at a radius of 1.0 km from the developing tornado.[13] The 1-km radius total circulation generally increased from 2148 to 2156, decreased slightly through 2158, then increased again by 2200 (Fig. 8). This increase in circulation, during the period when the SRFD had begun to surge east and north of the developing tornado, immediately preceded the increase in tornado intensity (Fig. 8). A decrease in the total circulation from 2156 to 2158 preceded a weakening of the tornado and corresponded to a decrease in the surge of SRFD air east of the tornado. The subsequent increase in circulation after 2158, corresponding to a reinvigorated SRFD surge, preceded the reintensification of the tornado.

Backward trajectories were calculated for the parcels that exited the 1-km-radius circulation to determine their source regions. Parcels were tracked backward from 2150 to 2142, 2152 to 2142, 2154 to 2142, 2156 to 2144, 2158 to 2146, 2200 to 2148, and 2202 to 2150.[14] Parcels originated along or just north of the FFGF, and mostly south of the LRR, for all times (Fig. 14a). These parcels initially traveled quasi horizontally, then slightly ascended as they approached the updraft associated with the low-level circulation, and finally descended as they became part of the downdraft. Horizontal vorticity and tilting were enhanced along the trajectories near the forward flank (Fig. 13). It is surmised that parcels entering the tornado then traveled through the regions of enhanced stretching and tilting that developed proximal to the tornado, associated with the eastward-surging SRFD.[15]

Forward trajectory calculations showed that parcels reaching the 1-km radius ring followed different types of paths thereafter. Parcels initialized on the northern and eastern segments of the ring were ingested by the developing tornado. The parcels south of the tornado became part of the rear–forward flow, initially moving eastward and then ascending the PRFGF to heights of several kilometers. Some of the parcels originating west of the ζ maximum followed similar paths and ascended near the PRFGF, while others, in particular the parcels on the periphery of the rear–forward flow adjacent to low-level updraft, were ingested by the tornado (Fig. 14b).

RK85, WW95, and Wakimoto et al. (1998) also found a significant number of parcels originating from the northeast, near the FFGF, entering tornadoes and/or low-level mesocyclones, thus underscoring the importance of this region for the development of low-level rotation. Importantly, the modeling results of RK85 and

[11] The dual-Doppler geometry was excellent and the scans in this analysis were synchronized better than in previous cases, so the inability to extract tilting along parcels' paths likely is due to the temporal evolution between dual-Doppler analyses and the lack of radar observations below 100–200 m AGL.

[12] The possibility that parcels experienced substantial amounts of integrated tilting during long passages through unresolvedly low-magnitude tilting cannot be excluded. However, observed changes in tornado intensity are well correlated with the observed changes in near-tornado tilting fields.

[13] A Lagrangian analysis of circulation along a material circuit was precluded, as a significant number of parcels along the 1-km ring frequently did not exit the circulation and therefore could not be tracked backward, leading to an incomplete material circuit.

[14] Most trajectories dropped below the data horizon (usually 200 m) after a couple of minutes, necessitating the use of downward extrapolation (see appendix for methodology). Even parcels that started at heights of 800 m dropped below the data horizon.

[15] It was difficult to trace the origins of many parcels reaching the 1-km ring in the eastern sector starting at 2156 much beyond the 1-km ring because these parcels often failed to sufficiently exit the near-tornado circulation.

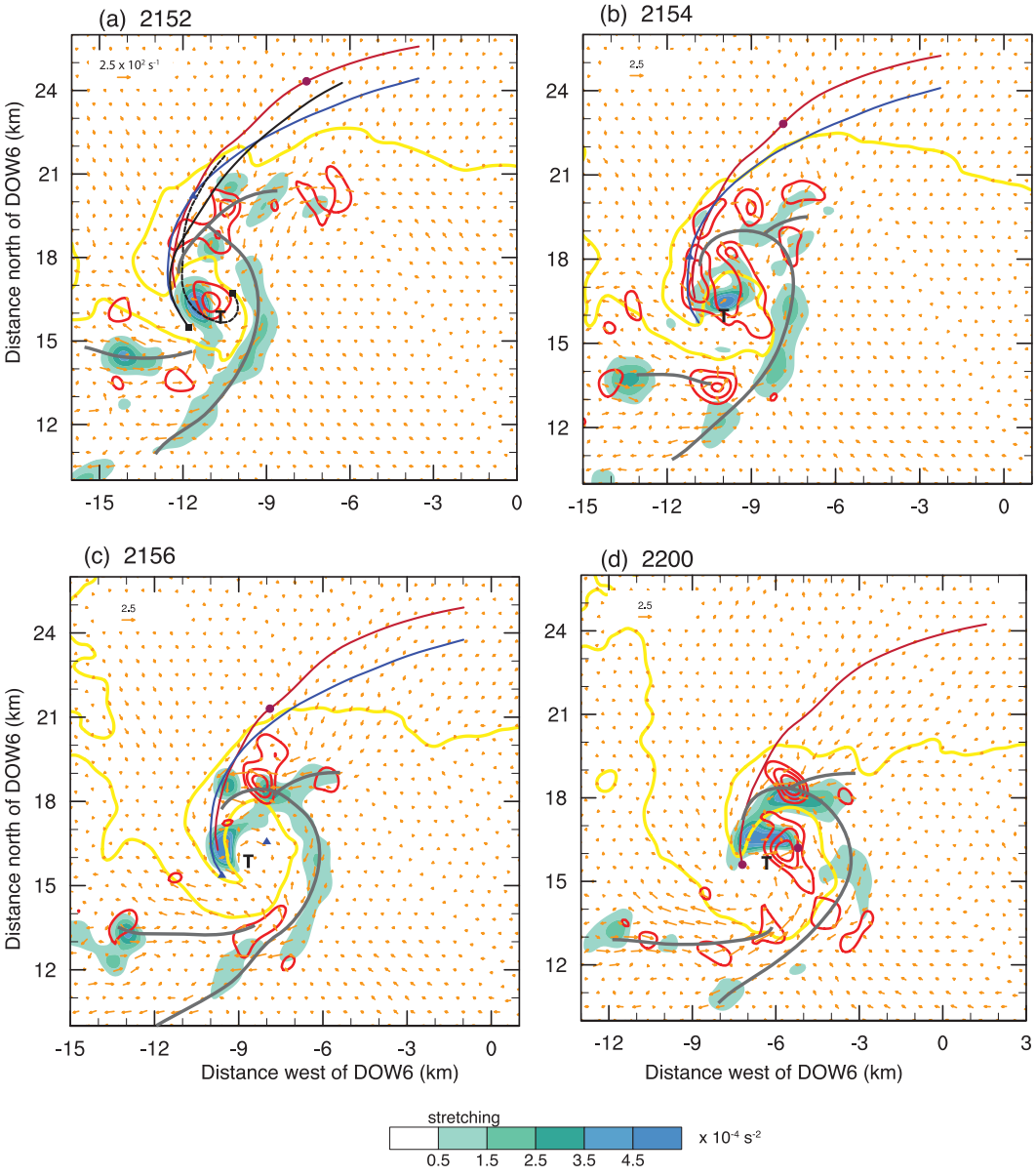

FIG. 13. Representative backward trajectories starting on the 1-km radius from 2200 to 2148 (maroon line), 2156 to 2144 (blue line), and 2152 to 2142 (black lines). Colored markers denote the location of these parcels at (a) 2152, (b) 2154, (c) 2156, and (d) 2200. The yellow line denotes the 30-dBZ DOW7 isopleth, orange arrows depict $\boldsymbol{\omega}_h$, red line contours denote positive tilting, and shading denotes stretching at each time. Tilting is contoured every 1.0 × 10^{-4} s^{-2}. All fields are shown at 0.3-km height. Tornado location is denoted with "T" and the location of the gust fronts are outlined in gray.

WW95 indicated a tilting of $\boldsymbol{\omega}_h$ as the parcels descended and then approached the mesocyclone from the east and appreciable stretching as the parcels were ingested into the mesocyclone. The dual-Doppler analyses of the Garden City, Kansas, storm by Wakimoto et al. (1998) did not show tilting along the trajectories' path, but appreciable stretching was observed as they neared the FFGF. It was hypothesized that the tilting process was present, but poorly resolved in their observations. WW95 identified an additional source region of parcels to the northwest of the tornado that also were ingested by the tornadic circulation. These parcels experienced greater vertical excursions than the parcels entering from the northeast. The environment of the storm modeled in WW95 was different from that of the currently studied storm, with larger storm-relative helicity,

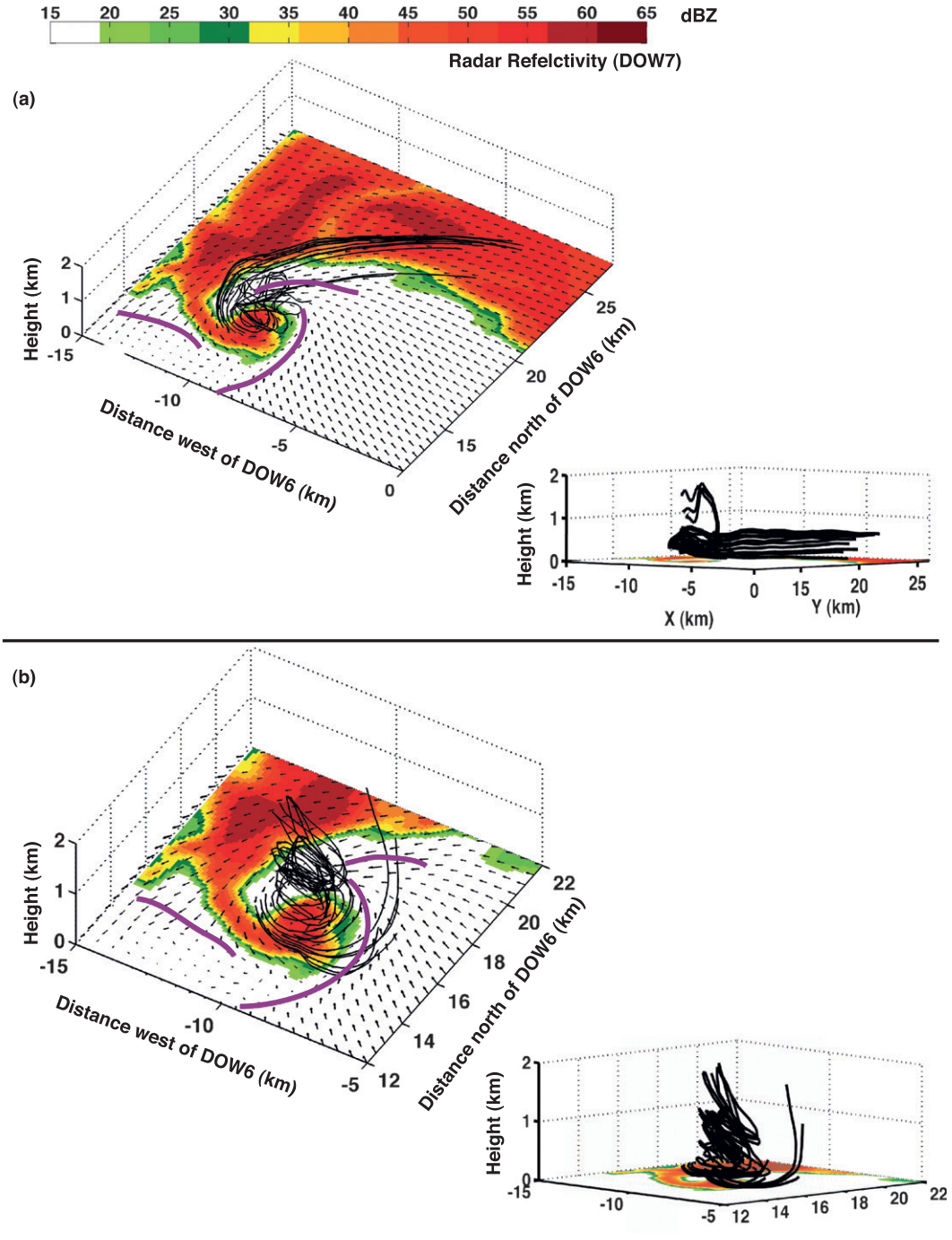

FIG. 14. (a) Backward trajectories from 2154 to 2142 starting at a radius of 1.0 km centered on the low-level ($z = 0.3$ km) ζ maximum (black lines). Parcels composing the 1-km circulation originate near the forward flank. (b) Forward trajectory paths from 2154 to 2202 starting at a radius of 1.0 km centered on the 0.3-km ζ maximum (black lines). Parcels composing the 1-km circulation generally were captured by the tornado, but some moved upward along the PRFGF, near the tornado. DOW7 reflectivity is contoured, vectors depict the horizontal winds at 0.3 km, and purple lines denote the locations of the gust fronts. The view is from the southeast.

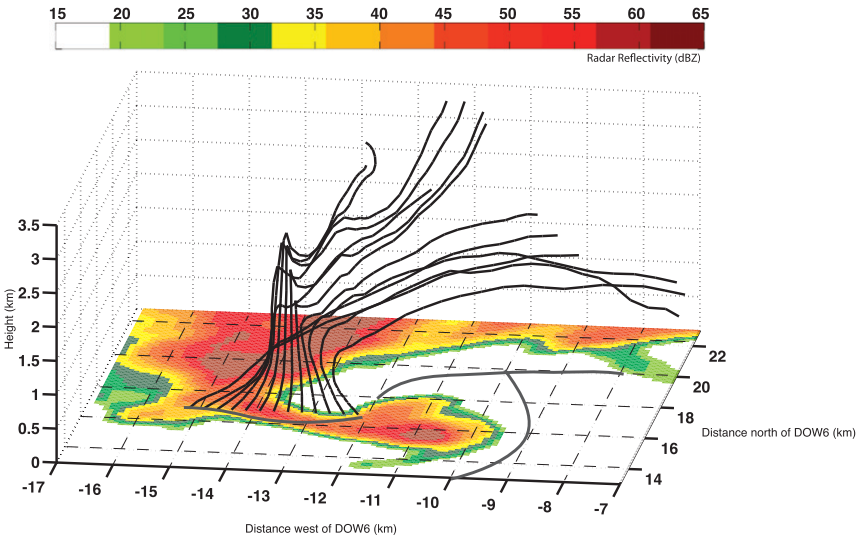

FIG. 15. Backward trajectories starting at 2152 and ending at 2142 for parcels starting just north of the SRFGF. Parcels that composed the SRFD originated a few km aloft. Radar reflectivity is shown at 0.3 km and gray lines denote the locations of the gust fronts. The view is from the south-southeast.

more CAPE, and a different hodograph shape, possibly resulting in differences in structures and, hence, horizontal source regions.[16] The results of the current analysis suggest that similar processes contributed to the genesis of the Goshen County tornado: generation of horizontal vorticity along the FFGF, subsequent tilting of this horizontal vorticity into the vertical on the east side of the circulation, and then stretching of the ζ by strong low-level convergence. The onset of strong low-level convergence, tilting, and stretching was associated with the onset of the surging SRFD. The evolution of these fields was well correlated with changes in tornado intensity (Fig. 8).

Since the SRFD surge led to increased convergence, tilting, and stretching that promoted tornadogenesis, it was of interest to ascertain the origins of the SRFD. The air behind the SRFGF comprised parcels originating from both the forward-flank and RFD regions, originating from heights of 0.5 to 3.0 km (Fig. 15). Parcels farther to the east were from the forward flank, whereas parcels farther to the west were associated with mainly downward motion. At 2152, MM observations revealed decreasing θ_e, from east to west across the hook echo (342–339 K), suggesting that air on the west side of the hook echo originated farther aloft (Fig. 16). Proximity sounding data from 2150 indicate that θ_e dropped below 339 K above 1 km (to a minimum of 325 K at 2 km). Assuming the conservation of moist entropy, these observations suggest that parcels in the SRFD originated from at least 1 km AGL, consistent with the results of L11 and M12 and the current trajectory analysis (Fig. 15). Most parcels from the SRFD did not enter the tornadic circulation, but instead ascended along the rear-flank gust fronts.

5. Conclusions

Finescale radar, thermodynamic, and photographic observations were integrated to provide a multiparameter analysis of the tornadogenesis process in a significant tornado. This dataset provided the unique opportunity to examine the role of an SRFD and other finescale features in tornadogenesis. Below is a summary of the processes observed during the genesis phase of the Goshen County tornado, and the deduced relationships between the observed processes, tornadogenesis, and early evolution of tornado intensity (Fig. 17):

1) During the approximately 10-min period corresponding to the tornadogenesis phase, the tornado-scale vortex underwent a strengthening phase, a subsequent weakening phase during which tornadogenesis

[16] Other discrepancies could have been due to the current dual-Doppler analysis starting at a height of about 200 m AGL, whereas the numerical study of WW95 extended much lower, below the levels observed by the DOWs (dual-Doppler fields were extrapolated below grid levels of 200 m prior to 2148 and below 100–200 m afterward), or because of frictional and microphysical effects, which were not properly accounted for in the numerical model.

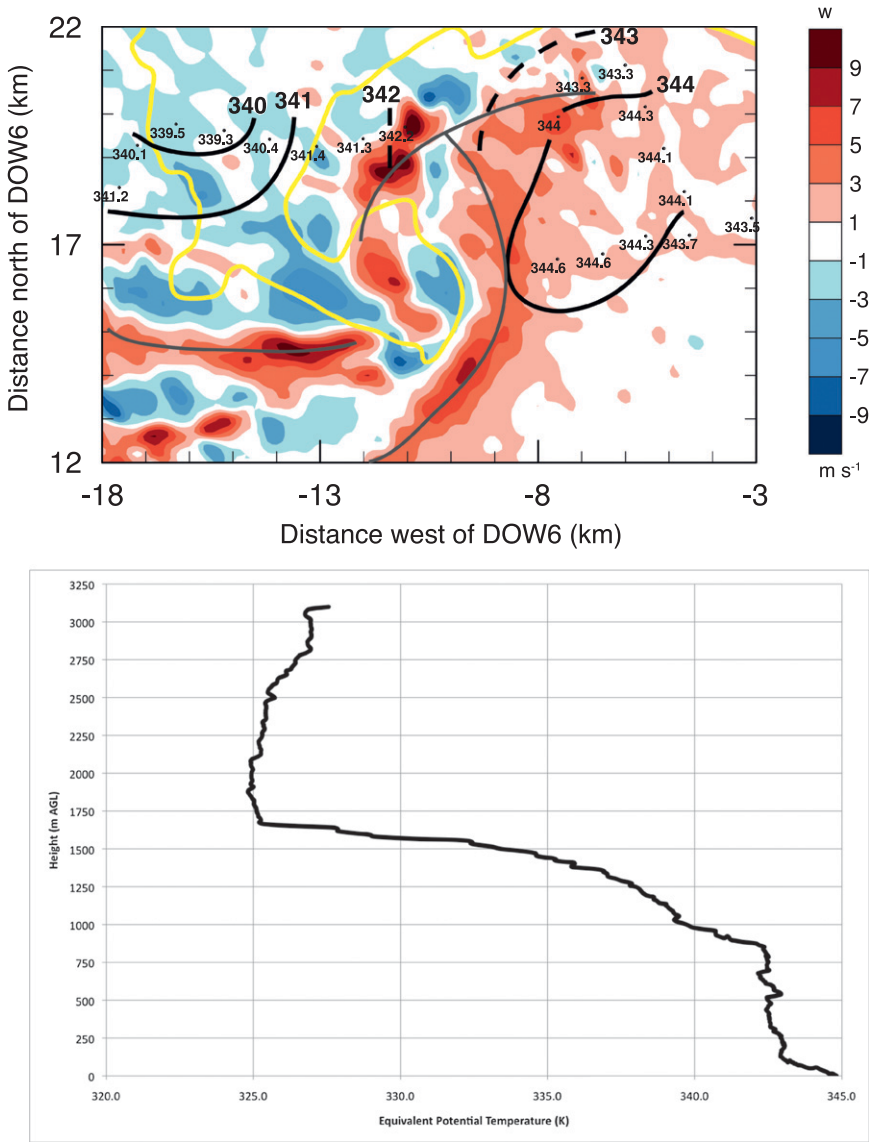

FIG. 16. (top) The θ_e (black isopleths; dashed isopleths indicate uncertainty in position) calculated from MM observations (black numbers), relative to the 30-dBZ DOW7 reflectivity (yellow isopleth), vertical motion (color contours), and gust fronts (gray lines) for 2152. Across the hook, near-surface θ_e decreased from east to west. Comparisons of θ_e values from MM and rawinsonde observations from the (bottom) 2150:26 sounding were consistent with the dual-Doppler trajectory analysis that indicates that downdraft air in this region originates from ≥1 km aloft.

stalled, and then a restrengthening phase. These changes closely followed changes in the magnitude of the SRFD, which developed west of the pretornadic circulation and wrapped cyclonically around the developing tornado. The two strengthening phases and one weakening phase of tornado intensity shortly following changes in downdraft strength, tilting, stretching, and total circulation suggest these changes were causative, not coincidental.

2) Trajectory analysis showed that parcels ingested by the tornadic circulation traversed the forward flank of the storm, where buoyancy gradients and associated horizontal vorticity were present near the surface. This suggests that parcels entering the tornado first acquired baroclinically generated horizontal vorticity during their residence within the forward flank, which was subsequently tilted and stretched along the SRFGF (i.e., the downstream

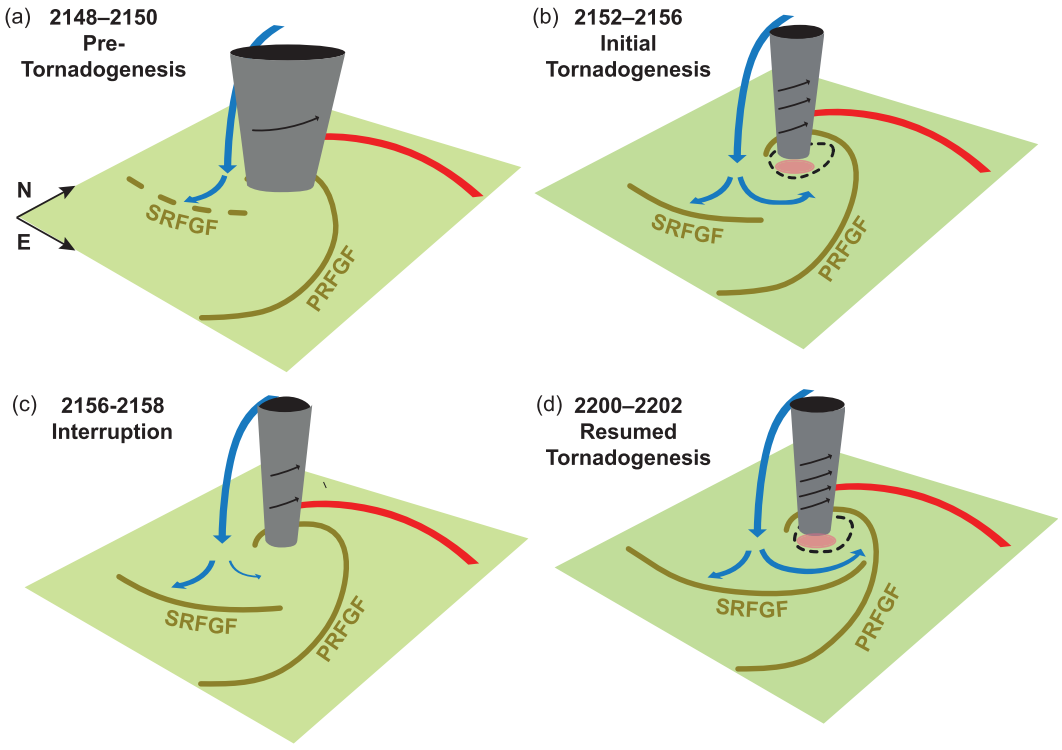

FIG. 17. (a)–(d) Schematic of the tornadogenesis process from 2148 to 2202. Blue lines indicate the strength and orientation of the SRFD, olive lines indicate the location and strength of the PRFGF and the SRFGF, and red lines indicate the FFGF. Enhanced convergence, associated with increased tilting (dashed black lines) and stretching (pink shading) occurs in (b) and (d). Changes in the SRFD were linked to enhanced production of ζ, tornadogenesis, brief weakening, and resumed intensification of the tornado. Intensity of the developing tornado is indicated schematically with the number of black arrows.

edge of the SRFD) just east of the ζ maximum. Changes in the SRFD characteristics near the tornado affected the tilting and stretching of vorticity, establishing conditions favorable for tornadogenesis. Although many of the parcels from the western sector followed a similar path, most did not enter the tornadic circulation; therefore, they did not directly affect tornadogenesis.

3) Vortex line arches in the outflow, joining the nascent tornadic circulation with an anticyclonic vortex that trailed the hook echo, were consistent with storm-generated baroclinic vorticity. During the tornadogenesis period, the MM-observed θ_v deficit along the baroclinic zone was only a few degrees, similar to other strong tornadic storms (MSR02; G07). A growing body of observations suggests that large instantaneous baroclinic generation of $\boldsymbol{\omega}_h$ may not be necessary for tornadogenesis. Instead, modest baroclinic generation of $\boldsymbol{\omega}_h$ over an extended time period in conjunction with a tilting (and subsequent stretching) mechanism near the low-level circulation center, as was observed to develop after 2150, may be most favorable for tornadogenesis.
4) A newly noticed reflectivity feature, the LRR, was first observed in this storm, and became quite pronounced immediately prior to tornadogenesis. Although the LRR was prominent in the reflectivity field, trajectory analysis showed that parcels entering the tornado did not pass through it, and it had no obvious link to the processes that contributed to tornadogenesis.
5) Visual manifestations of features associated with the developing tornado were well correlated with those resolved in the single- and dual-Doppler analyses. The frequently (visually) observed unsteady process of tornado intensification during genesis, including the formation and dissipation of funnels during genesis, was associated with kinematic properties of this storm resolved in the radar analysis. Specifically, a prominent near-surface anticyclonic vortex developed just prior to tornadogenesis and was evident both in the radar and the photogrammetric observations. Minutes after the radar-measured circulation reached tornadic

intensity, a funnel cloud was visible aloft. Subsequently, the radar-measured circulation briefly decreased in intensity and had a disorganized multiple vortex structure. Correspondingly, the visible funnel disappeared and was replaced by two broad lowerings. When the radar-measured winds in the tornado again increased, the funnel reappeared and extended to near the ground. The tornado was observed by radar to form about 10 min before a visible condensation funnel reached the ground.

Strong rotation is observed frequently in nontornadic supercells (Trapp 1999; Beck et al. 2006; Markowski et al. 2011); therefore, the processes that are associated with the development of a low-level mesocyclone do not always result in tornadogenesis. While the available data and wind synthesis necessarily limit the scope and certainty of the results, a potential triggering mechanism for tornadogenesis in this storm has been identified. Further evaluation of the hypothesized tornadogenesis/triggering mechanism will require the analysis of many more cases in varied storm environments and with different analysis techniques and data. For example, data assimilation modeling experiments may extend these results to explore aspects of tornadic and nontornadic storms that have not been observed directly.

Acknowledgments. The authors thank the VORTEX2 crews, PIs, and Steering Committee for their devotion to the collection of these very important datasets and the reviewers for their comments, which we feel substantially improved the manuscript. The authors thank David Dowell for reviewing an earlier draft of this work. The National Science Foundation provided support for this analysis through AGS-0801041, AGS-1211132, AGS-0801035, and AGS-1157646 for VORTEX2 planning through AGS-0724318, and for the DOWs through AGS-0734001.

APPENDIX

Radar Sampling and Analysis Techniques

The DOWs were single-polarization systems in 2009, operating near 9.37 GHz with a transmit power of 250 kW, and pulse lengths and gate lengths were matched at 0.4 μs (60 m). Volumetric data collection commenced after the DOWs were leveled to within 0.1°, as determined by both pedestal-mounted bubble levels and gravimetric inclinometers.

The DOW6–DOW7 dual-Doppler baseline was 15.41 km. The crossing angle of the DOW6 and DOW7 beams through the tip of the hook at 2142 was 34.4°, suitable for dual-Doppler analysis, and increased as the storm moved toward the radars. At 2142, the lowest-elevation radar beams (0.5°) crossed through the tip of the hook at 170–200 m above the height of the individual radars. However, since the terrain at this location was ~1640 m MSL, higher than the altitude of the DOWs, these beams were only 50–130 m AGL. After 2148, the tip of the hook and the mesocyclone had moved over lower terrain, typically 1500–1550 m AGL, and the height of the lowest radar beams from 2148 to 2202 was about 100 m AGL.

The DOWs scanned at ~50° s^{-1}, azimuthally oversampling radar beams every ~0.5°, completing volume scans every 120 s (revisiting low elevations approximately every 60 s), and yielding 19 dual-Doppler volumes from 2142 to 2218. Additionally, data were collected by DOW7 from 2130 to 2142, by DOW6 from 2218 to 2226, and Rapid-Scan volumetric data were collected at 7-s intervals from 2202 to 2234. Elevation angles of 0.5°, 1°, 2°, 3°, 4°, 5°, 6°, 8°, 10°, 12°, 14°, and 16° were used for both DOWs in the wind syntheses.

Azimuthal rotation (yaw) for each DOW was determined by aligning ~50 man-made clutter targets in 0.5° and 1.0° radar sweeps, resulting in an accuracy of ~0.1°, much less than the ~0.5° azimuthal sampling interval. Scan timing between DOW6 and DOW7 was synchronized so that scans through low levels and higher levels of the storm were nearly contemporaneous, especially during the genesis period of 2148–2202, minimizing errors in the dual-Doppler analysis caused by storm evolution between the observation times of the radars.

Data were interpolated to a Cartesian grid using a two-pass Barnes (Koch et al. 1983) scheme (Barnes 1964) using a second-pass convergence parameter γ of 0.30 (Majcen et al. 2008). Grid parameters were based on the azimuthal δ_h and vertical δ_v data spacing at the average location of the mesocyclone. For a conservative oversampled half-power beamwidth of 0.7° and an elevation interval of 1° at a range of 20 km, this resulted in δ_h = 244 m and δ_v = 349 m. A smoothing parameter [$\kappa = (1.33\delta)^2$] of 0.216 km^2 (Pauley and Wu 1990) and a grid spacing ($\Delta = \delta/2.5$) of 100 m were chosen (Koch et al. 1983) over a 30 km × 30 km horizontal and 4-km (early) and 1.5-km (late) vertical domain. No downward extrapolation was performed in the objective analysis. Grid coordinates were relative to DOW6.

Plotted dual-Doppler winds were mesocyclone-relative. A mesocyclone motion of $(u, v) = (10.6, -2.8)$ m s^{-1} was determined using averaged DOW-measured low-level mesocyclone locations during 2143–2203. Vertical velocities were derived from upward integration of the anelastic mass continuity equation with a lower boundary

condition of $w = 0$. Dual-Doppler fields were extrapolated downward from the lowest observed level (typically 200 m above the lowest grid level) using downward propagation of the coefficients of the directional cosine terms of the dual-Doppler equation and iteratively solving for u, v, and w. The lowest grid level was at the level of DOW6, 1568 m MSL. Terrain height was as much as 70 m higher under the mesocyclone before 2148, but more typically within ±50 m.

Trajectories were computed using a fourth-order Runge–Kutta integration scheme and trilinear spatial interpolation at 20-s intervals. Since retrieved ω_h was noisy, likely because of errors in w, a three-step Leise (1982) filter was applied to the three-dimensional vorticity field during vortex line calculation. Trajectories and vortex line calculations began at $z = 300$ m, 100–200 m above the lowest level of nonextrapolated observations, but trajectories were allowed to drop below 300 m.

REFERENCES

Adlerman, E. J., 2003: Numerical simulations of cyclic storm behavior: Mesocyclogenesis and tornadogenesis. Ph.D. dissertation, University of Oklahoma, 217 pp. [Available from School of Meteorology, University of Oklahoma, 100 East Boyd, Suite 1310, Norman, OK 73019.]

——, K. K. Droegemeier, and R. Davies-Jones, 1999: A numerical simulation of cyclic mesocyclogenesis. *J. Atmos. Sci.,* **56,** 2045–2069.

Alexander, C., and J. Wurman, 2005: The 30 May 1998 Spencer, South Dakota, storm. Part I: The structural evolution and environment of the supercell tornadoes. *Mon. Wea. Rev.,* **133,** 72–96.

——, and ——, 2008: Updated mobile radar climatology of supercell tornado structures and dynamics. Preprints, *24th Conf. on Severe Local Storms,* Savannah, GA, Amer. Meteor. Soc., 19.3. [Available online at https://ams.confex.com/ams/pdfpapers/142112.pdf.]

Atkins, N. T., A. McGee, R. Ducharme, R. M. Wakimoto, and J. Wurman, 2012: The LaGrange tornado during VORTEX2. Part II: Photogrammetric analysis of the tornado combined with dual-Doppler radar data. *Mon. Wea. Rev.,* **140,** 2939–2958.

Barnes, S. L., 1964: A technique for maximizing details in numerical weather map analysis. *J. Appl. Meteor.,* **3,** 396–409.

Beck, J. R., J. L. Schroeder, and J. M. Wurman, 2006: High-resolution, dual-Doppler analyses of the 29 May 2001 Kress, Texas, cyclic supercell. *Mon. Wea. Rev.,* **134,** 3125–3148.

Biggerstaff, M. I., and Coauthors, 2005: The Shared Mobile Atmospheric Research and Teaching radar: A collaboration to enhance research and teaching. *Bull. Amer. Meteor. Soc.,* **86,** 1263–1274.

Brandes, E. A., 1977: Gust front evolution and tornado genesis as viewed by Doppler radar. *J. Appl. Meteor.,* **16,** 333–338.

——, 1978: Mesocyclone evolution and tornadogenesis: Some observations. *Mon. Wea. Rev.,* **106,** 995–1011.

——, 1981: Finestructure of the Del City-Edmond tornadic mesocirculation. *Mon. Wea. Rev.,* **109,** 635–647.

——, 1984: Vertical vorticity generation and mesoscyclone sustenance in tornadic thunderstorms: The observational evidence. *Mon. Wea. Rev.,* **112,** 2253–2269.

Byko, Z., P. Markowski, Y. Richardson, J. Wurman, and E. Adlerman, 2009: Descending reflectivity cores in supercell thunderstorms observed by mobile radars and in a high-resolution numerical simulation. *Wea. Forecasting,* **24,** 155–186.

Davies-Jones, R., 2008: Can a descending rain curtain in a supercell instigate tornadogenesis barotropically? *J. Atmos. Sci.,* **65,** 2469–2497.

——, and H. Brooks, 1993: Mesocyclogenesis from a theoretical perspective. *The Tornado: Its Structure, Dynamics, Prediction, and Hazards, Geophys. Monogr.,* Vol. 79, Amer. Geophys. Union, 105–114.

——, R. J. Trapp, and H. B. Bluestein, 2001: Tornadoes and tornadic storms. *Severe Convective Storms, Meteor. Monogr.,* No. 50, Amer. Meteor. Soc., 167–222.

Dowell, D. C., and H. B. Bluestein, 1997: The Arcadia, Oklahoma, storm of 17 May 1981: Analysis of a supercell during tornadogenesis. *Mon. Wea. Rev.,* **125,** 2562–2582.

——, and ——, 2002a: The 8 June 1995 McLean, Texas, storm. Part I: Observations of cyclic tornadogenesis. *Mon. Wea. Rev.,* **130,** 2626–2648.

——, and ——, 2002b: The 8 June 1995 McLean, Texas, storm. Part II: Cyclic tornado formation, maintenance, and dissipation. *Mon. Wea. Rev.,* **130,** 2649–2670.

Finley, C. A., B. D. Lee, M. Grzych, C. D. Karstens, and T. M. Samaras, 2010: Mobile mesonet observations of the rear-flank downdraft evolution associated with a violent tornado near Bowdle, SD on 22 May 2010. Preprints, *25th Conf. on Severe Local Storms,* Denver, CO, Amer. Meteor. Soc., 8A.2. [Available online at https://ams.confex.com/ams/pdfpapers/176132.pdf.]

Fujita, T. T., 1981: Tornadoes and downbursts in the context of generalized planetary scales. *J. Atmos. Sci.,* **38,** 1511–1534.

——, and R. M. Wakimoto, 1982: Anticyclonic tornadoes in 1980 and 1981. Preprints, *12th Conf. on Severe Local Storms,* San Antonio, TX, Amer. Meteor. Soc., 213–216.

Grzych, M. L., B. D. Lee, and C. A. Finley, 2007: Thermodynamic analysis of supercell rear-flank downdrafts from Project ANSWERS. *Mon. Wea. Rev.,* **135,** 240–246.

Heymsfield, G. M., 1978: Kinematic and dynamic aspects of the Harrah tornadic storm analyzed from dual-Doppler radar data. *Mon. Wea. Rev.,* **106,** 233–254.

Hirth, B. D., J. L. Schroeder, and C. C. Weiss, 2008: Surface analysis of the rear-flank downdraft outflow in two tornadic supercells. *Mon. Wea. Rev.,* **136,** 2344–2363.

Klemp, J. B., and R. Rotunno, 1983: A study of the tornadic region within a supercell thunderstorm. *J. Atmos. Sci.,* **40,** 359–377.

——, R. B. Wilhelmson, and P. S. Ray, 1981: Observed and numerically simulated structure of a mature supercell thunderstorm. *J. Atmos. Sci.,* **38,** 1558–1580.

Koch, S. E., M. desJardins, and P. J. Kocin, 1983: An interactive Barnes objective map analysis scheme for use with satellite and conventional data. *J. Climate Appl. Meteor.,* **22,** 1487–1503.

Kosiba, K. A., and J. Wurman, 2008: DOW observations of multiple vortex structure in several tornadoes. Preprints, *24th Conf. on Severe Local Storms,* Savannah, GA, Amer. Meteor. Soc., P3.20. [Available online at https://ams.confex.com/ams/pdfpapers/142194.pdf.]

Lee, B. D., C. A. Finley, and T. M. Samaras, 2011: Surface analysis near and within the Tipton, Kansas, tornado on 29 May 2008. *Mon. Wea. Rev.,* **139,** 370–386.

Lee, W.-C., and J. Wurman, 2005: The diagnosed structure of the Mulhall tornado. *J. Atmos. Sci.,* **62,** 2373–2393.

Leise, J. A., 1982: A multidimensional scale-telescoped filter and data extension package. NOAA Tech. Memo. ERL WRL-82, 19 pp. [Available from NOAA Office of Oceanic and Atmospheric Research, Silver Spring Metro Center, Bldg. 3, Room 11627, Silver Spring, MD 20910.]

Lemon, L. R., and C. A. Doswell, 1979: Severe thunderstorm evolution and mesocyclone structure as related to tornadogenesis. *Mon. Wea. Rev.,* **107,** 1184–1197.

Majcen, M., P. Markowski, Y. Richardson, D. Dowell, and J. Wurman, 2008: Multipass objective analyses of Doppler radar data. *J. Atmos. Oceanic Technol.,* **25,** 1845–1858.

Markowski, P. M., 2002: Hook echoes and rear-flank downdrafts: A review. *Mon. Wea. Rev.,* **130,** 852–876.

——, and Y. P. Richardson, 2009: Tornadogenesis: Our current understanding, forecasting considerations, and questions to guide future research. *Atmos. Res.,* **93,** 3–10.

——, J. M. Straka, and E. N. Rasmussen, 2002: Direct surface thermodynamic observations within the rear-flank downdrafts of nontornadic and tornadic supercells. *Mon. Wea. Rev.,* **130,** 1692–1721.

——, ——, and ——, 2003: Tornadogenesis resulting from the transport of circulation by a downdraft: Idealized numerical simulations. *J. Atmos. Sci.,* **60,** 795–823.

——, E. Rasmussen, J. Straka, R. Davies-Jones, Y. Richardson, and R. J. Trapp, 2008: Vortex lines within low-level mesocyclones obtained from pseudo-dual-Doppler radar observations. *Mon. Wea. Rev.,* **136,** 3513–3535.

——, M. Majcen, Y. Richardson, J. Marquis, and J. Wurman, 2011: Characteristics of the wind field in a trio of nontornadic low-level mesocyclones observed by the Doppler on Wheels radars. *Electron. J. Severe Storms Meteor.,* **5** (7). [Available online at http://www.ejssm.org/ojs/index.php/ejssm/article/view/75/63.]

——, and Coauthors, 2012a: The pretornadic phase of the Goshen County, Wyoming, supercell of 5 June 2009 intercepted by VORTEX2. Part I: Evolution of kinematic and surface thermodynamic fields. *Mon. Wea. Rev.,* **140,** 2887–2915.

——, Y. Richardson, J. Marquis, R. Davies-Jones, J. Wurman, K. Kosiba, P. Robinson, and E. Rasmussen, 2012b: The pretornadic phase of the Goshen County, Wyoming, supercell of 5 June 2009 intercepted by VORTEX2. Part II: Intensification of low-level rotation. *Mon. Wea. Rev.,* **140,** 2916–2938.

Marquis, J., Y. Richardson, J. Wurman, and P. Markowski, 2008: Single- and dual-Doppler analysis of a tornadic vortex and surrounding storm scale flow in the Crowell, TX, supercell of 30 April 2000. *Mon. Wea. Rev.,* **136,** 5017–5043.

——, ——, P. Markowski, D. Dowell, and J. Wurman, 2012a: Tornado maintenance investigated with high-resolution dual-Doppler and EnKF analysis. *Mon. Wea. Rev.,* **140,** 3–27.

——, ——, ——, ——, ——, K. Kosiba, and P. Robinson, 2012b: An investigation of the tornadic stage of the Goshen County, Wyoming, supercell of 5 June 2009 using EnKF assimilation of mobile radar data collected during VORTEX2. Preprints, *26th Conf. on Severe Local Storms,* Nashville, TN, Amer. Meteor. Soc., 169. [Available online at https://ams.confex.com/ams/26SLS/webprogram/Paper211344.html.]

Parker, M. D., 2012: Impacts of lapse rates upon low-level rotation in idealized storms. *J. Atmos. Sci.,* **69,** 538–559.

Pauley, P. M., and X. Wu, 1990: The theoretical, discrete, and actual response of the Barnes objective analysis scheme for one- and two-dimensional fields. *Mon. Wea. Rev.,* **118,** 1145–1163.

Rasmussen, E. N., M. S. Gilmore, and R. Davies-Jones, 2006: A preliminary survey of rear-flank descending reflectivity cores in supercell storms. *Wea. Forecasting,* **21,** 923–928.

Ray, P. S., 1976: Vorticity and divergence fields within tornadic storms from dual-Doppler observations. *J. Appl. Meteor.,* **15,** 879–890.

——, R. J. Doviak, G. B. Walker, D. Sirmans, J. Carter, and B. Bumgarner, 1975: Dual-Doppler observation of a tornadic storm. *J. Appl. Meteor.,* **14,** 1521–1530.

——, B. C. Johnson, K. W. Johnson, J. S. Bradberry, J. J. Stephens, K. K. Wagner, R. B. Wilhelmson, and J. B. Klemp, 1981: The morphology of several tornadic storms on 20 May 1977. *J. Atmos. Sci.,* **38,** 1643–1663.

Richardson, Y. P., P. Markowski, J. N. Marquis, J. Wurman, K. A. Kosiba, P. Robinson, D. W. Burgess, and C. C. Weiss, 2012: Tornado maintenance and demise in the Goshen County, Wyoming supercell of 5 June 2009 intercepted by VORTEX2. Preprints, *26th Conf. on Severe Local Storms,* Nashville, TN, Amer. Meteor. Soc., 13.3. [Available online at https://ams.confex.com/ams/26SLS/webprogram/Paper212526.html.]

Rotunno, R., and J. B. Klemp, 1985: On the rotation and propagation of simulated supercell thunderstorms. *J. Atmos. Sci.,* **42,** 271–292.

Straka, J. M., E. N. Rasmussen, and S. E. Fredrickson, 1996: A mobile mesonet for finescale meteorological observations. *J. Atmos. Oceanic Technol.,* **13,** 921–936.

——, ——, R. P. Davies-Jones, and P. M. Markowski, 2007: An observational and idealized numerical examination of low-level counter-rotating vortices toward the rear flank of supercells. *Electron. J. Severe Storms Meteor.,* **2** (8). [Available online at http://www.ejssm.org/ojs/index.php/ejssm/article/view/32/33.]

Trapp, R. J., 1999: Observations of nontornadic low-level mesocyclones and attendant tornadogenesis failure during VORTEX. *Mon. Wea. Rev.,* **127,** 1693–1705.

Wakimoto, R. M., and H. Cai, 2000: Analysis of a nontornadic storm during VORTEX 95. *Mon. Wea. Rev.,* **128,** 565–592.

——, C.-H. Liu, and H. Cai, 1998: The Garden City, Kansas, storm during VORTEX 95. Part I: Overview of the storm's life cycle and mesocyclogenesis. *Mon. Wea. Rev.,* **126,** 372–392.

——, N. T. Atkins, and J. Wurman, 2011: The LaGrange tornado during VORTEX2. Part I: Photogrammetric analysis of the tornado combined with single-Doppler radar data. *Mon. Wea. Rev.,* **139,** 2233–2258.

——, P. Stauffer, W.-C. Lee, N. T. Atkins, and J. Wurman, 2012: Finescale structure of the LaGrange, Wyoming, tornado during VORTEX2: GBVTD and photogrammetric analyses. *Mon. Wea. Rev.,* **140,** 3397–3418.

Waugh, S., and S. E. Fredrickson, 2010: An improved aspirated temperature system for mobile meteorological observations, especially in severe weather. Preprints, *25th Conf. on Severe Local Storms,* Denver, CO, Amer. Meteor. Soc., P5.2. [Available online at https://ams.confex.com/ams/25SLS/webprogram/Paper176205.html.]

Wicker, L. J., and R. B. Wilhelmson, 1995: Simulation and analysis of tornado development and decay within a three-dimensional supercell thunderstorm. *J. Atmos. Sci.,* **52,** 2675–2703.

Wurman, J., 2001: The DOW mobile multiple-Doppler network. Preprints, *30th Int. Conf. on Radar Meteorology,* Munich,

Germany, Amer. Meteor. Soc., P3.3. [Available online at https://ams.confex.com/ams/pdfpapers/21572.pdf.]

——, 2002: The multiple vortex structure of a tornado. *Wea. Forecasting,* **17,** 473–505.

——, and S. Gill, 2000: Fine-scale radar observations of the Dimmitt, Texas, tornado. *Mon. Wea. Rev.,* **128,** 2135–2164.

——, and M. Randall, 2001: An inexpensive, mobile, rapid-scan radar. Preprints, *30th Conf. on Radar Meteorology,* Munich, Germany, Amer. Meteor. Soc., P3.4. [Available online at https://ams.confex.com/ams/pdfpapers/21577.pdf.]

——, J. Straka, and E. Rasmussen, 1996a: Fine-scale Doppler radar observation of tornadoes. *Science,* **272,** 1774–1777.

——, ——, and ——, 1996b: Preliminary radar observations of the structure of tornadoes. Preprints, *18th Conf. on Severe Local Storms,* San Francisco, CA, Amer. Meteor. Soc., 17–22.

——, ——, ——, M. Randall, and A. Zahrai, 1997: Design and deployment of a portable, pencil-beam, pulsed, 3-cm Doppler radar. *J. Atmos. Oceanic Technol.,* **14,** 1502–1512.

——, C. Alexander, P. Robinson, and Y. Richardson, 2007a: Low-level winds in tornadoes and potential catastrophic tornado impacts in urban areas. *Bull. Amer. Meteor. Soc.,* **88,** 31–46.

——, Y. Richardson, C. Alexander, S. Weygandt, and P. F. Zhang, 2007b: Dual-Doppler and single-Doppler analysis of a tornadic storm undergoing mergers and repeated tornadogenesis. *Mon. Wea. Rev.,* **135,** 736–758.

——, ——, ——, ——, and ——, 2007c: Dual-Doppler analysis of winds and vorticity budget terms near a tornado. *Mon. Wea. Rev.,* **135,** 2392–2405.

——, P. Robinson, W. Lee, C. R. Alexander, and K. A. Kosiba, 2008: Rapid-scan mobile radar 3D GBVTD and traditional analysis of tornadogenesis. Preprints, *24th Conf. on Severe Local Storms,* Savannah, GA, Amer. Meteor. Soc., P13.6. [Available online at https://ams.confex.com/ams/pdfpapers/142176.pdf.]

——, K. A. Kosiba, P. Markowski, Y. Richardson, D. Dowell, and P. Robinson, 2010: Finescale single- and dual-Doppler analysis of tornado intensification, maintenance, and dissipation in the Orleans, Nebraska, supercell. *Mon. Wea. Rev.,* **138,** 4439–4455.

——, D. Dowell, Y. Richardson, P. Markowski, E. Rasmussen, D. Burgess, L. Wicker, and H. Bluestein, 2012: The second Verification of the Origins of Rotation in Tornadoes Experiment: VORTEX2. *Bull. Amer. Meteor. Soc.,* **93,** 1147–1170.

——, K. A. Kosiba, and P. Robinson, 2013: In situ, Doppler radar, and video observations of the interior structure of a tornado and wind–damage relationship. *Bull. Amer. Meteor. Soc.,* in press.